An improved mean-field homogenization model for the three-dimensional elastic properties of masonry

Zhou, Yubao; Sluys, Lambertus J.; Esposito, Rita

DOI
10.1016/j.euromechsol.2022.104721

Publication date
2022

Document Version
Final published version

Published in
European Journal of Mechanics, A/Solids

European Journal of Mechanics / A Solids 96 (2022) 104721

Contents lists available at ScienceDirect

European Journal of Mechanics / A Solids

journal homepage: www.elsevier.com/locate/ejmsol

An improved mean-field homogenization model for the three-dimensional elastic properties of masonry

Yubao Zhou *, Lambertus J. Sluys, Rita Esposito

Department of Materials, Mechanics, Management and Design (3MD), Faculty of Civil Engineering and Geosciences, Delft University of Technology, 2628CN, Delft, The Netherlands

ARTICLE INFO

Keywords:
Masonry
Mean-field homogenization
Orthotropic stiffness tensor
Micromechanics

ABSTRACT

Accurate assessment of the overall mechanical behavior of masonry, composed of bricks and mortar joints, remains challenging due to its inhomogeneous and orthotropic nature. In this study, the feasibility of various mean-field homogenization schemes for the three-dimensional orthotropic elastic properties of masonry is comprehensively investigated. Three kinds of masonry patterns are considered, including the stack bonded pattern, the running bonded pattern and the double-leaf Flemish bonded pattern that has received limited attention so far. Special attention is paid to the homogenization schemes which have not been applied to the masonry case, such as Lielens' interpolative double inclusions (D-I) and the interaction direct derivative (IDD) schemes. After a comparison between the well-known mean-field homogenization schemes, an improved micro-mechanical model is proposed by combining the advantages of the IDD and D-I models. The validation of the proposed model is conducted through a comparison against experimental data from literature and numerical results obtained via finite element analyses (FEA). The results show that the proposed model can accurately evaluate the orthotropic elastic properties of the three masonry typologies for a wide range of stiffness ratios between brick and mortar, ranging from 1 to 1000. The proposed model also shows better performance than the classical schemes especially when the stiffness ratios between brick and mortar are higher than 10, which is of major importance for the application of mean-field homogenization based multiscale methods to the nonlinear analysis of masonry. Furthermore, the presented homogenization method can be of interest for other anisotropic materials, e.g., laminate materials.

1. Introduction

For the purpose of housing safety of still-in-use masonry buildings and the protection of ancient architectures, it is essential to thoroughly understand the mechanical behavior of masonry structures and provide accurate assessment of their resilience against different loads (e.g., gravity, wind and earthquake). Nevertheless, it is still a significant challenge to characterize masonry material and conduct structural analysis accordingly even if masonry is generally not seen as a high-tech material (Rekik and Lebon, 2012). This complexity mainly stems from the composite nature of masonry showing heterogeneous and anisotropic behavior. Specifically, masonry is generally deemed as a two-phase material composed of units and mortar or a three-phase material by further considering the interface between the units and mortar (Rekik and Lebon, 2012; Lourenço and Rots, 1997). The heterogeneous behavior of masonry is characterized by the different properties of constituents and complicated interaction between them. The highly orthotropic behavior arises from different geometric arrangement of units (Kumar et al., 2016), and from the much lower stiffness of mortar than that of units especially for ancient masonry structures (Almeida and Lourenço, 2020).

In view of the complexity involved in the material characterization of masonry composite, extensive experimental and modelling work is present in literature (Adam et al., 2010; Chang et al., 2020, 2021, 2022; Drougkas et al., 2015a, 2016; Jafari et al., 2020; Kaushik et al., 2007; Lourenco et al., 2007; Page, 1978). A comprehensive experimental material characterization of existing masonry is often not performed, because it is costly and hindered by the invasiveness of testing methods required to determine the complete orthotropic nonlinear behavior (Jafari et al., 2022). Among the modelling approaches, the brick-to-brick modelling provides the most detailed description by modelling every brick separately connected by interfaces (Louren ç o

* Corresponding author.
E-mail addresses: Y.Zhou-16@tudelft.nl (Y. Zhou), L.J.Sluijs@tudelft.nl (L.J. Sluys), R.Esposito@tudelft.nl (R. Esposito).

https://doi.org/10.1016/j.euromechsol.2022.104721
Received 29 September 2021; Received in revised form 10 April 2022; Accepted 24 June 2022
Available online 29 June 2022

and Rots, 1997) or contact elements (D' Altri et al., 2019); nevertheless the high computational costs make its application to structural analysis of buildings limited. As an alternative, homogenization-based approaches become increasingly popular among the masonry community (Zucchini and Louren ç o, 2002). Homogenization approaches are aimed at deriving the composite behavior from a representative volume element (RVE) that contains the geometries and constitutive relations of the individual constituents and offers a continuum description of the composite (Dormieux et al., 2006). The masonry composites can then be assumed effectively homogeneous by determining the macro stresses and strains of the RVE.

Over the last decades, many numerical, semi-analytical and analytical homogenization models for masonry have been proposed, each with its advantages and limitations (Almeida and Louren ç o, 2020; Lourenco et al., 2007). The numerical homogenization models, based on finite element (FE) representation of masonry RVE, have been widely reported to evaluate both linear and nonlinear response of masonry (Page, 1978; Anthoine, 1995; Cecchi and Sab, 2002; Hu and Tuohuti, 2014; Massart et al., 2004). This method can accurately describe the interaction between the constituents and the macro stresses and strains of the RVE (Drougkas et al., 2015b), which, therefore, has been used by several researchers as benchmark to validate analytical models (Zucchini and Louren ç o, 2002; Cecchi and Sab, 2002; Drougkas et al., 2015b). For computational efficiency, several semi-analytical or reduced order approaches were developed for masonry in the past decade. One of the most used semi-analytical approaches for masonry homogenization is the transformation field analysis (TFA) that considers the inelastic strain as uniform in the region of the RVE, characterized by nonlinear response (Dvorak, 1992). The TFA-based homogenization procedures have been extensively adopted to study both the in-plane and out-of-plane nonlinear response of periodic masonry by Sacco and co-workers (Chettah et al., 2013; Sacco, 2009; Addessi and Sacco, 2012; Addessi et al., 2010, 2020, 2021; Marfia and Sacco, 2012; Sacco et al., 2010). Recently, Almeida & Lourenço (Almeida and Louren ç o, 2020) investigated the feasibility of a new semi-analytical multiscale modelling technique called mechanics of structure genome (MSG) for masonry homogenization. It was observed that the results obtained by this semi-analytical method are in agreement with those of various comparative methods with a much lower computational cost with respect to a full FE solution. Almeida & Cecchi (Almeida and Cecchi, 2021) further applied the MSG technique to the homogenization of masonry reinforced by fiber reinforced polymer (FRP). It was observed that the results obtained by the MSG agreed with those from a 3D FE benchmark. For a full analytical approach, different closed-form solutions have been proposed since the 1950's (Bati et al., 1999). A two-step analysis procedure was usually adopted by early analytical homogenization models (Louren ç o, 1996; Maier et al., 1991; Pande et al., 1989; Pietruszczak and Niu, 1992). In such cases, masonry was deemed as layered materials, in which the head and bed joints are homogenized in sequence. These "two-step" models cannot distinguish between different masonry typologies and the homogenization results always depend on the step order (Kumar et al., 2016; Zucchini and Louren ç o, 2002; Wang et al., 2007). Another type of closed-form solution to the masonry homogenization is the micromechanical modelling developed by (Zucchini and Louren ç o, 2002; Drougkas et al., 2015b; Taliercio, 2014). Based on internal deformation mechanisms, such models assemble the stress equilibrium and strain compatibility conditions into a collection of closed-form equations which can then be solved in a single analysis step.

Among various homogenization methods, the mean-field homogenization technique provides a cost-effective way to derive the global properties of the composite from its micro-structures (Pierard et al., 2004). Following the solutions to the matrix-inclusion problem by Eshelby (1957) and Laws (1977), several mean-field homogenization models have been proposed. By imposing that the size of the heterogeneity is one scale lower than the size of a RVE of the continuum material, the strain of the continuum material can be calculated as average strain by considering linear displacements, periodic boundary conditions or uniform traction at the boundary of the volume (Nemat-Nasser and Hori, 2013). The global stiffness tensor of the composite can thus be determined by considering the elastic tensors of constituents and the concentration tensor related to the inclusions which contain information regarding their shapes, orientations and volume concentrations.

Due to the simple averaging method proposed by the mean-field homogenization technique, it has been adopted to evaluate the overall behaviors of various composite-like materials (Pierard et al., 2004; Deude et al., 2002; Doghri et al., 2016; Fritsch et al., 2013; Morin et al., 2017; Pardoen and Hutchinson, 2003; Pens é e et al., 2002; Pichler et al., 2007; Ulm et al., 2004; Zhu et al., 2009). However, the application of this technique to masonry has received very limited attention. The feasibility of mean-field techniques to predict the three-dimensional elastic response of masonry has not yet been comprehensively examined. The first application of mean-field homogenization technique to masonry was carried out by Pietruszczak & Niu (Pietruszczak and Niu, 1992), who arrived at the homogenization through two successive steps. The Mori-Tanaka scheme was applied first where the head joints are approximated by elliptic cylinders. The derived effective medium was then homogenized with the bed mortar joints by using the periodic layered homogenization method. This procedure, as mentioned above, is one of the "two-step" models which introduce several errors. Bati et al. (1999) proposed a single-step homogenization procedure, with the bricks being approximated by aligned elliptic cylindrical inclusions embedded in the surrounding mortar matrix. The authors validated the plausibility of such elliptical cylinder assumption through a comparison with experimental data. However, this work only focused on the derivation of in-plane elastic constants. Moreover, only the running bonded pattern was considered, thus ignoring other possible masonry typologies. Wang et al. (2007) adopted the periodic eigenstrain homogenization method for masonry homogenization. The disturbance field caused by the constituents was derived by Fourier series, which is similar to the Eshelby's tensor of an inclusion-matrix system (Eshelby, 1957). Likewise, the formation of this model was also limited to in-plane loading characteristics and only considered the single leaf structures (i.e., stack and running bonded masonry). Kumar et al. (2016) applied the self-consistent scheme (SCS) to running bonded masonry, where the analytical model was compared with an FE solution. The authors investigated the influence of the stiffness ratio between constituents and the thickness of mortar on the overall elastic behavior of masonry composites. It was found that the analytical results obtained by the SCS scheme were close to the FE results, but the model validation was restricted to the Young's moduli in three directions, thus ignoring shear moduli and Poisson's ratios. Recently, Drougkas & Sarhosis (Drougkas and Sarhosis, 2021) proposed a micro-mechanical model for the prediction of elastic stiffness and compressive strength of three-leaf masonry by adopting the mean-field homogenization theory. In this model, the dilute scheme was used, with the bricks and stones being approximated as ellipsoids which were embedded in an infinite mortar matrix. However, the prediction results for the vertical Young's modulus from the proposed model showed large differences with respect to the experimental data.

This study comprehensively investigates the feasibility and accuracy of different mean-field homogenization schemes for the evaluation of the orthotropic elastic properties of three different masonry typologies, including the stack bonded, running bonded and double-leaf Flemish bonded masonry. The Flemish bonded pattern represents a significant part of masonry structures but has received limited attention in literature. Eight homogenization schemes are investigated, including those are not considered in previous works, such as Lielens' interpolative double inclusions (D-I), interaction direct derivative (IDD) and effective self-consistent (ESCS) schemes. A wide range of stiffness ratios between brick and mortar, ranging from 1 to 1000, is considered to assess the performance of each homogenization scheme for inelastic behavior. After a comparison between the well-known schemes, an improved

model is proposed by combining the advantages of the IDD and D-I models. The proposed model can account for the geometry and properties of each microscopic phase and the global geometry of the RVE at the same time. This allows to approximate the distribution of each inclusion in the RVE to some extent. Therefore, compared to the classical mean-field homogenization schemes, the proposed model is more suitable for the approximation of the orthotropic masonry-like materials with a periodical distribution of microscopic phases. Validations of the proposed model is conducted by a comparison against FE benchmark and experimental results obtained from literature.

2. Research significance and objectives

The application of mean-field homogenization technique for the prediction of effective elastic properties of masonry has not yet been comprehensively examined. The available reported literature was mainly restricted to the derivation of Young's moduli of running bonded masonry using the dilute, MT and SCS homogenization schemes by considering bricks as elliptical cylindrical or ellipsoidal inclusions. These results ignored the study of shear moduli and Poisson's ratios, the response of different masonry patterns and a comprehensive investigation on the choice of the inclusion phase (to be selected between bricks and mortar). Differently, in this study a wider range of mean-field homogenization schemes is considered predicting all the elastic constants of different masonry patterns including an investigation on different inclusion-matrix assumptions. In addition, for the application of mean-field homogenization to masonry, the available reported literature was restricted to the situations of a limited stiffness ratio between brick and mortar less than 30. Considering the broader scope of developing an analytical based multiscale model for masonry, a wide range of stiffness ratios between brick and mortar, ranging from 1 to 1000, is considered in present study to assess the performance of each homogenization scheme for inelastic behavior. These findings can thus be of relevance for other orthotropic materials such as cross-ply laminates.

This study presents the first step towards developing an analytically based multiscale model for masonry. As a simple and efficient upscaling method, the mean-field homogenization technique has been successfully applied to many analytical or semi-analytical multiscale methods by combining it with different damage, plasticity or fracture models at macro and microscale, for the nonlinear analyses of various isotropic composite materials in different fields ranging from metal composites (Doghri et al., 2016), alloys (Pardoen and Hutchinson, 2003), rocks (Deude et al., 2002; Pens é e et al., 2002), cementitious materials (Pichler et al., 2007; Ulm et al., 2004), geomaterials (Zhu et al., 2009) and bones (Fritsch et al., 2013; Morin et al., 2017). These analytical or semi-analytical multiscale procedures achieve a balance between the accuracy and computational cost, and their implementation to simulate structural behavior is considered feasible. However, such application to masonry is limited. The main problem pending is the error of the orthotropic effective elastic tensor of masonry introduced by the classical mean-field homogenization schemes when large differences in stiffness between brick and mortar are expected. This issue is obvious in the case of nonlinear analysis, where the tangent stiffness of one or both components gradually tends to zero with increasing inelastic behavior. The improved mean-filed homogenization model proposed in present study accurately predicts the stiffness tensors of masonry composites for a wide range of stiffness ratios between brick and mortar, ranging from 1 to 1000, and thus has the potential to be incorporated to the well-established multiscale models to achieve the nonlinear analysis of masonry. One of the potential nonlinear extensions is to apply the model developed in present study to the so-called microporomechnics theory (Dormieux et al., 2006). By combining the mean-field homogenization technique and the linear elastic fracture mechanics theory, the microporomechnics theory has been successfully used to explain phenomena such as failure of rock (Barth é l é my et al., 2003; Zhu et al., 2008) and degradation of concrete (Esposito and Hendriks, 2016). Furthermore, it has been shown that, by adopting the microporomechnics theory, the nonlinear response of quasi-brittle material as concrete can be predicted based on a limited number of parameters, mainly the elastic and strength values (Esposito and Hendriks, 2015, 2016). This become of paramount importance for masonry that requires a large number of tests for its characterization, which cannot often be performed for existing structures (Jafari, 2021).

3. Definition of RVEs for selected masonry typologies

Three masonry typologies, including stack, running and Flemish bonded patterns, are considered in this study. For a clear discussion, a right-hand Cartesian frame is defined. The bed joint (i.e., horizontal direction), head joint (i.e., vertical direction) and the direction of wall thickness (i.e., transversal direction) align with the x, y and z axis, respectively. The RVE term was first used by Hill (1963) and it is descibed as the smallest material volume element for which the macroscopic constitutive representation is a sufficiently accurate model to represent mean constitutive response (Drugan and Willis, 1996). Although in general the RVE notion is not easy to define, for ordered materials as masonry, the RVE can be defined as the element which completely decribes the structure by periodicity. Therefore, the RVE shall be selected/modelled such that duplicating it provides sufficient accuracy of representing the material's larger scales (Omairey et al., 2019). In this study, the masonry RVE is derived by properly selecting a periodic unit cell in which the microstructures can be described exactly. The selected stack bonded RVE contains one completed stretcher brick and the surrounding mortar joints, which can be further discretized into bed, head and cross joints. The cross joints are here defined as the volume of mortar joints at the intersection between head and bed joints (Fig. 1a). The running bonded RVE is formed by four half-sized stretcher bricks with mortar joints between them (Fig. 1b). The Flemish bonded RVE is discretized into one completed header brick, four quarter-sized header bricks and eight half-sized stretcher bricks surrounded by four kinds of mortar joints (i.e., bed, head, cross and collar joints), as shown in Fig. 1c. The dimensions of masonry constituents are designated as follows: l_b, h_b and t_b are the length, height and thickness of the units, and l_m, h_m and t_m are the thickness of head, bed and collar mortar joints, respectively.

4. State-of-the-art for mean-field homogenization

Following the solution provided by Eshelby (1957) for the elastic matrix-inclusion problem, several models for composite materials have been proposed, creating a new field which can be named as Eshelbian-based continuum micromechanics. By considering an inclusion embedded in an infinite elastic matrix that is subjected to homogeneous boundary conditions (uniform displacement or uniform tractions), the effective (macroscopic) stiffness tensor $\boldsymbol{C}^*$ and compliance tensors $\boldsymbol{D}^*$ can be expressed in the following forms:

$$\boldsymbol{C}^* = \boldsymbol{C}_m + \sum_i c_i(\boldsymbol{C}_i - \boldsymbol{C}_m) : \boldsymbol{A}_i \tag{1a}$$

$$\boldsymbol{D}^* = \boldsymbol{D}_m + \sum_i c_i(\boldsymbol{D}_i - \boldsymbol{D}_m) : \boldsymbol{B}_i \tag{1b}$$

To be clear from the context, tensors are designated by boldface symbols and a colon is used to denote the tensor operation for double dot product. For a matrix-inclusion system, the matrix and the inclusion of type-i are labeled by m and i, respectively. $\boldsymbol{C}_m$, $\boldsymbol{D}_m$ and $\boldsymbol{C}_i$, $\boldsymbol{D}_i$ are the stiffness and compliance tensors of matrix material and type-i inclusion, respectively. c_m and c_i are the volume fractions of the surrounding matrix and type-i inclusion, respectively. $\boldsymbol{A}_i$ and $\boldsymbol{B}_i$ are the average strain and stress concentration tensors, respectively. The strain and stress over type-i inclusion ($\langle\boldsymbol{\varepsilon}\rangle_{\Omega_i}$ and $\langle\boldsymbol{\sigma}\rangle_{\Omega_i}$) and the macroscopic applied ones ($\boldsymbol{E}$ and $\boldsymbol{\Sigma}$) can be linked by $\boldsymbol{A}_i$ and $\boldsymbol{B}_i$:

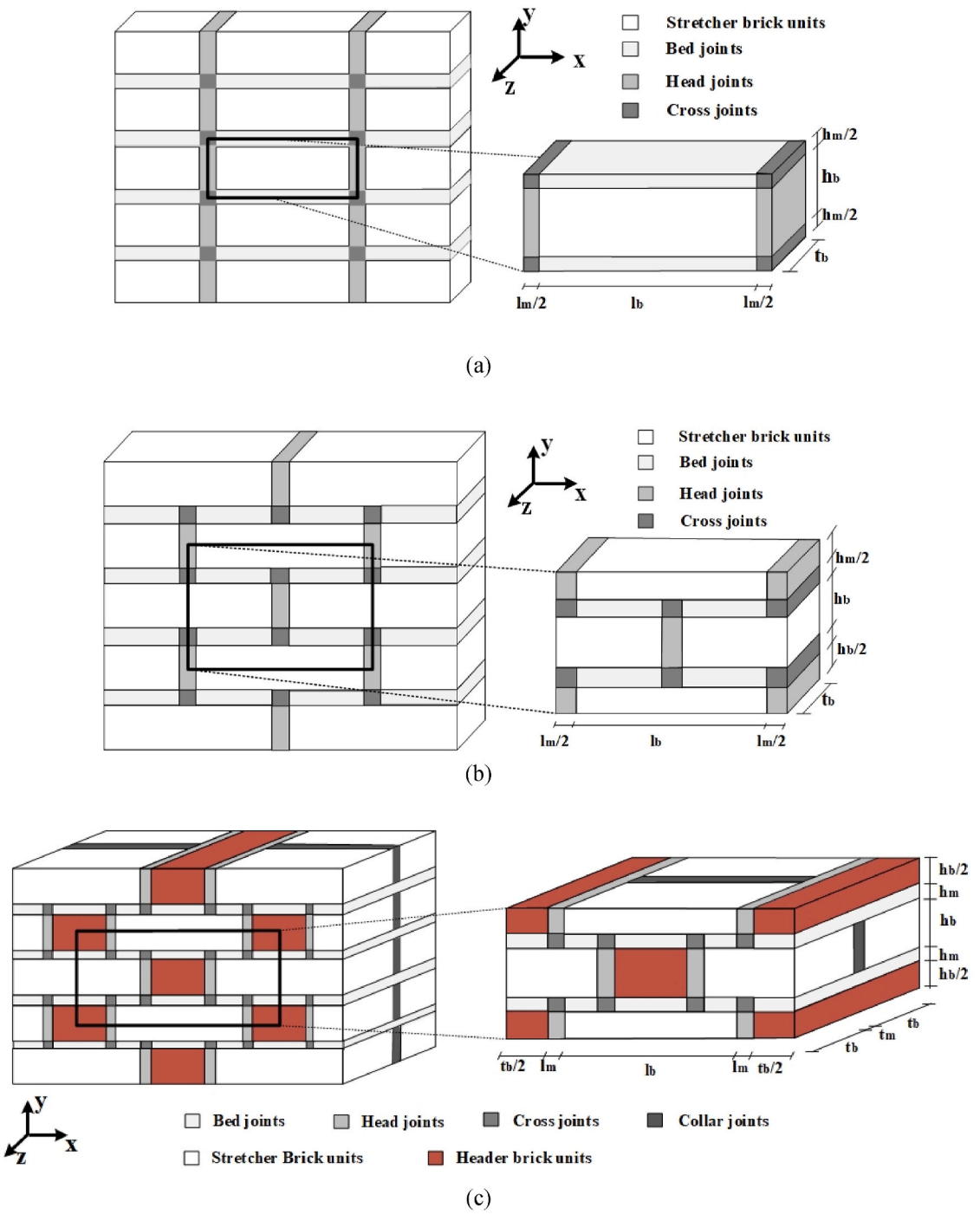

Fig. 1. Derivation of the masonry RVEs: (a) stack bonded; (b) running bonded; (c) Flemish bonded.

$$\langle \boldsymbol{\varepsilon} \rangle_{\Omega_i} = \boldsymbol{A}_i : \boldsymbol{E} \tag{2a}$$

$$\langle \boldsymbol{\sigma} \rangle_{\Omega_i} = \boldsymbol{B}_i : \boldsymbol{\Sigma} \tag{2b}$$

Various homogenization schemes adopt different expressions of $\boldsymbol{A}_i$ and $\boldsymbol{B}_i$ to evaluate the interaction degree between matrix and inclusions. The Voigt and Reuss schemes assume uniform strain and uniform stress in the RVE, respectively, thus ignoring the interaction between phases (Pierard et al., 2004). The dilute scheme also ignores the interactions between phases under the assumption that each inclusion is embedded in an unbounded matrix in isolate (Mura, 2013). The Mori-Tanaka (MT) scheme and self-consistent scheme (SCS) are developed based on the dilute scheme to further consider the interactions between inclusions. The MT scheme allows for slight interactions between inclusions by assuming that each type-i inclusion is sequentially embedded in the surrounding matrix (Benveniste, 1987). In the assumption of the SCS method, each inclusion is directly embedded in the homogenized effective medium with the unknown stiffness tensor $\boldsymbol{C}^*$ (Klusemann and Svendsen, 2010). The effective self-consistent scheme (ESCS) and the interaction direct derivative (IDD) schemes are developed on the basis of three-phase model (Zheng and Du, 2001). The ESCS scheme assumes that each inclusion (Ω_i) is first embedded into a finite matrix (Ω_m) and then the type-i inclusion-matrix cell denoted by Ω_{Di}, with $\Omega_{Di} = \Omega_i + \Omega_m$, is embedded in the infinite homogenized effective medium denoted by Ω^E with unknown effective (macro) stiffness tensor $\boldsymbol{C}^*$. However, the implementation of the implicit ESCS requires an additional iterative

loop and this scheme can only provide a reasonable approximation for low stiffness and low volume fraction (Klusemann and Svendsen, 2010). Therefore, the IDD scheme was proposed as an explicit version of the ESCS scheme. Different from the assumption of the ESCS scheme, the type-i inclusion-matrix cell Ω_{Di} is embedded in the infinite surrounding matrix denoted by Ω^m in the assumption of the IDD scheme (Zheng and Du, 2001; Du and Zheng, 2002).

The expressions of $\boldsymbol{A}_i$ and/or $\boldsymbol{B}_i$ for some classical mean-field homogenization schemes are summarized in Table 1, where $\boldsymbol{I}$ is the fourth-order symmetric identity tensor. $\boldsymbol{S}_i^m$ and $\boldsymbol{S}_i^*$ are the Eshelby tensors which contain the geometric information of type-i inclusion. Likewise, $\boldsymbol{S}_{Di}^m$ and $\boldsymbol{S}_{Di}^*$ are the Eshelby tensors of type-i inclusion-matrix cell for the ESCS and IDD schemes. The labels m and $*$ imply that the Eshelby tensor is calculated according to the Poisson's ratio of the matrix ν_m and of the effective composite materialν^*, respectively.

Another classical scheme named as double inclusions (D-I) model was proposed by selecting an appropriate interpolation between the stiffness estimates from the MT and inverse MT schemes (Pierard et al., 2004; Lielens, 1999). The effective stiffness $\boldsymbol{C}^{*(D-I)}$ is determined as follow:

$$\boldsymbol{C}^{*(D-I)} = \left\{ (1 - 1/2c_I(1+c_I))\left[\boldsymbol{C}^{*(MT)}\right]^{-1} + 1 \Big/ 2c_I(1+c_I)\left[\boldsymbol{C}^{*\left(MT^{-1}\right)}\right]^{-1} \right\}^{-1} \tag{3}$$

where $c_I = \sum_i c_i$ is sum of the volume fractions of all inclusion families; $\boldsymbol{C}^{*(MT)}$ and $\boldsymbol{C}^{*(MT^{-1})}$are the estimation of macro stiffness tensors from the MT and the inverse MT schemes, respectively. The inverse MT scheme corresponds to MT model where the matrix and inclusions are permuted for two-phase materials (Pierard et al., 2004).

5. Proposed homogenization-based model for masonry

Fig. 2 provides a physical interpretation for the aforementioned homogenization schemes. Consider a fictitious two-phase material with a specific geometry shown in Fig. 2a. Generally, to make a precise prediction for the effective elasticity of two-phase materials, information concerning property and geometry (shape and orientation) of each phase, as well as global geometry of the RVE (the matrix-inclusion cell), is needed. The Voigt and Reuss schemes only consider the elastic properties and ignore all the geometric information. Although the dilute, MT and SCS schemes further account for the geometry of the inclusion phase, the information concerning the geometries of the matrix phase and the RVE is lost (Fig. 2b). The ESCS and IDD methods successfully account for the global geometric information of the RVE which is included in the Eshelby tensors of the matrix-inclusion cell ($\boldsymbol{S}_{\mathrm{Di}}^*$ and $\boldsymbol{S}_{\mathrm{Di}}^m$), but the geometric information of the matrix phase is still missing (Fig. 2c). Although the D-I model better reveals the geometric information of a two-phase material by simultaneously considering the geometries of both inclusion and matrix phases, it however fails to account for the global geometry of the RVE (Fig. 2d).

Consequently, an improved homogenization approach can be proposed by the combination of the ideas of the D-I and IDD models. The D-I model was proposed according to the fact that the real properties of composites are closer to the MT estimate for small volume fraction of inclusions c_I and closer to the inverse MT estimate for large c_I (Lielens, 1999). The stiffness estimate of the D-I model is obtained by selecting an appropriate interpolation between the MT estimate and the inverse MT estimate (Eq. (3)), which is therefore close to the real properties of composites for both small and large volume fractions of inclusions. From the viewpoint of physical meanings, the IDD method can be seen as a more advanced model with respect to the MT scheme to further consider the global geometry of the RVE. For the IDD method, the Eshelby tensor $\boldsymbol{S}_{\mathrm{Di}}^m$ is calculated based on the aspect ratio of RVE (matrix-inclusion cell) and the Eshelby tensor $\boldsymbol{S}_i^m$ is calculated based on the aspect ratio of inclusion phase (Fig. 2c). In most cases when the aspect ratio of RVE is different from that of the inclusion phase, i.e., $\boldsymbol{S}_{\mathrm{Di}}^m \neq \boldsymbol{S}_i^m$, the stiffness estimates from the IDD and MT method are different. However, for a special case when the composite RVE has the same aspect ratio as the inclusion phase, i.e., $\boldsymbol{S}_{\mathrm{Di}}^m = \boldsymbol{S}_i^m$, the stiffness estimates from the IDD and MT methods are identical. In such special case, by replacing the $\boldsymbol{S}_{\mathrm{Di}}^m$ with $\boldsymbol{S}_i^m$ in the expression of stress concentration tensor of the IDD scheme $\boldsymbol{B}_i^{(IDD)}$ (Table 1), the expression of $\boldsymbol{B}_i^{(IDD)}$ will be transformed into Eq. (4), which is equal to that of the MT scheme $\boldsymbol{B}_i^{(MT)}$ (see also (Zheng and Du, 2001; Weng, 1990)).

$$\begin{aligned} \boldsymbol{B}_i^{(IDD)} &= \boldsymbol{B}_i^{(Dilute)} : \left[\boldsymbol{I} - \sum_i c_i (\boldsymbol{D}_i - \boldsymbol{D}_m) : \boldsymbol{B}_i^{(Dilute)} : \boldsymbol{C}_m : \left(\boldsymbol{I} - \boldsymbol{S}_i^m\right) \right]^{-1} \\ &= \boldsymbol{B}_i^{(MT)}, \text{ if } \ \boldsymbol{S}_{\mathrm{Di}}^m = \boldsymbol{S}_i^m \end{aligned} \tag{4}$$

The homogenization approach developed in present study is obtained by applying the interpolation function of D-I model to the IDD and inverse IDD estimates. For a two-phase material, the IDD estimate can be obtained by choosing the smaller volume part as the inclusion phase. Alternatively, by selecting the larger volume part as inclusion phase leads to another approximation of the average stress concentration tensor $\boldsymbol{B}_i^{(IDD^{-1})}$ and corresponding macro compliance tensor $\boldsymbol{D}^{*(IDD^{-1})}$. This is here after called the inverse IDD model.

$$\boldsymbol{D}^{*\left(IDD^{-1}\right)} = \boldsymbol{D}_i + c_m(\boldsymbol{D}_m - \boldsymbol{D}_i) : \boldsymbol{B}_i^{\left(IDD^{-1}\right)} \tag{5}$$

By properly choosing an interpolation between the IDD and the inverse IDD estimates, a new homogenization model is established as follows:

$$\boldsymbol{C}^{*(New)} = \left[(1 - \zeta(c_I))\boldsymbol{D}^{*(IDD)} + \zeta(c_I)\boldsymbol{D}^{*\left(IDD^{-1}\right)} \right]^{-1} \tag{6}$$

where $\boldsymbol{C}^{*(New)}$ is the stiffness estimate of the proposed model. $\zeta(c_I)$ is a smooth function of interpolation which satisfies the following conditions (Pierard et al., 2004):

Table 1
Expressions of average strain concentration tensor $\boldsymbol{A}_i$ and/or average stress concentration tensor $\boldsymbol{B}_i$ for some classical mean-field homogenization schemes.

Scheme	$\boldsymbol{A}_i$	$\boldsymbol{B}_i$
Voigt	$\boldsymbol{I}$	–
Reuss	–	$\boldsymbol{I}$
Dilute	$[\boldsymbol{I} + \boldsymbol{S}_i^m : \boldsymbol{C}_m^{-1} : (\boldsymbol{C}_i - \boldsymbol{C}_m)]^{-1}$	$\boldsymbol{C}_i : \boldsymbol{A}_i^{(Dilute)} : \boldsymbol{D}_m$
MT	$\boldsymbol{A}_i^{(Dilute)} : \left(c_m \boldsymbol{I} + \sum_i c_i \boldsymbol{A}_i^{(Dilute)}\right)^{-1}$	$\boldsymbol{B}_i^{(Dilute)} : \left(c_m \boldsymbol{I} + \sum_i c_i \boldsymbol{B}_i^{(Dilute)}\right)^{-1}$
SCS	$[\boldsymbol{I} + \boldsymbol{S}_i^* : \boldsymbol{C}^{*-1} : (\boldsymbol{C}_i - \boldsymbol{C}^*)]^{-1}$	$\boldsymbol{C}_i : \boldsymbol{A}_i^{(SCS)} : \boldsymbol{D}^*$
ESCS	–	$\boldsymbol{B}_i^{(Dilute)} : [\boldsymbol{I} - \boldsymbol{C}^* : (\boldsymbol{I} - \boldsymbol{S}_{\mathrm{Di}}^*) : (\boldsymbol{D}^* - \boldsymbol{D}_m)]^{-1}$
IDD	–	$\boldsymbol{B}_i^{(Dilute)} : \left[\boldsymbol{I} - \sum_i c_i (\boldsymbol{D}_i - \boldsymbol{D}_m) : \boldsymbol{B}_i^{(Dilute)} : \boldsymbol{C}_m : (\boldsymbol{I} - \boldsymbol{S}_{\mathrm{Di}}^m) \right]^{-1}$

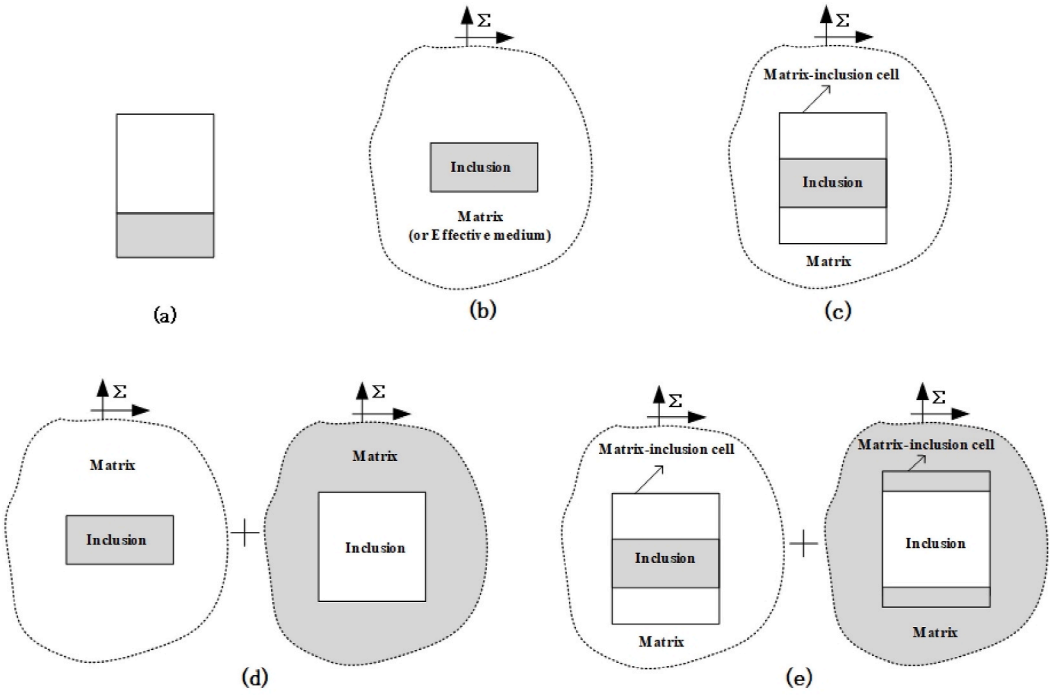

Fig. 2. Schematic illustration for the physical interpretation of different homogenization models: (a) specific geometry of a fictitious two-phase material; (b) dilute, MT and SCS models; (c) IDD method; (d) D-I model; (e) the proposed model.

$$\zeta(c_I) > 0\ , \frac{\mathrm{d}\zeta}{\mathrm{d}v_I}(c_I) > 0, \lim_{v_I \to 0}\zeta(c_I) = 0, \lim_{v_I \to 1}\zeta(c_I) = 1 \tag{7}$$

The simple quadratic expression for $\zeta(c_I)$ proposed by Lielens (1999) is adopted in this study:

$$\zeta(c_I) = \frac{1}{2}c_I(1 + c_I) \tag{8}$$

The proposed model combines the advantages of the IDD and D-I models and thus is able to account for the microscopic geometry of each phase and the global geometry of the RVE at the same time, as shown in Fig. 2e. From the viewpoint of physical meanings, the proposed model can also be seen as an improved version of D-I model to further consider the global geometries of the composite RVE and the containment relationship between each microscopic phase and its corresponding matrix-inclusion cell (RVE). This allows to consider the distribution of each inclusion to some extent, leading to a more accurate approximation for the real behavior of the RVE. With the condition $\boldsymbol{S}_{\mathrm{D}i}^{m} = \boldsymbol{S}_{i}^{m}$, the stiffness estimate of the proposed model is equal to that of the D-I model.

The proposed model and other classical mean-field homogenization schemes have been applied to the stack, running and Flemish bonded masonry RVEs. The derivation of an explicit expression for the Eshelby's tensor is possible only for simple shapes of the inclusions such as sphere, ellipsoid, penny shaped and cylinder (Mura, 2013). Bati et al. (1999) approximated the brick units by elliptical cylindrical inclusions, where the feasibility of such hypothesis has also been validated against experiments by the authors. Accordingly, in this study, the inclusions are considered as elliptical cylinders. The expression of Eshelby tensor for elliptic cylindrical inclusions is shown in Appendix A.

For the dilute, MT, SCS and IDD schemes, two options for the matrix-inclusion system are studied. One possible option considers mortar joints as elliptical cylindrical inclusions, which are embedded in an infinite brick matrix (Fig. 3a). Another option treats the bricks as elliptical cylindrical inclusions and the mortar joints are considered as matrix phase (Fig. 3b). Following the naming rule of the MT and inverse MT models (Lielens, 1999), the model corresponding to the assumption that considers the mortar as inclusions is named as the scheme itself (i.e., the dilute, MT, SCS and IDD), while the inverse model corresponds to the assumption considering the bricks as inclusions (i.e., the inverse dilute, inverse MT, inverse SCS and inverse IDD). Additionally, the inverse MT model corresponds to the model adopted by Bati et al. (1999), the inverse dilute model corresponds to the model adopted by Drougkas & Sarhosis (Drougkas and Sarhosis, 2021) and the inverse SCS model corresponds to the model used by Kumar et al. (2016). There is no difference between the Voigt or Reuss model and the inverse Voigt or inverse Reuss model, because the aspect ratios of microscopic phases in the composites has not been considered. The inverse ESCS model is invalid, as the concentration of the brick inclusions is far beyond its numerical limit of 0.5 (Klusemann and Svendsen, 2010). Fig. 3c gives the assumptions of matrix-inclusion system for the proposed model, where each elliptical cylindrical inclusion is first embedded into a matrix-inclusion cell (RVE) that is also idealized as an elliptical cylinder. The elliptical cylindrical matrix-inclusion cell is then embedded into the infinite matrix. For the IDD, ESCS and the proposed models, the inclusion phase and corresponding matrix-inclusion cell (RVE) should be idealized as the same type (both idealized as elliptical cylinders in present study), otherwise the estimate of effective stiffness tensor would be physically unacceptable (Zheng and Du, 2001). If the inclusion phase and corresponding matrix-inclusion cell (RVE) are idealized as different types (e.g., elliptical cylindrical inclusion and ellipsoidal matrix-inclusion cell), negative values of the effective Young's moduli are obtained that are not physically possible.

The stiffness estimate of the proposed model strongly depends on the selection and calculation of the Eshelby tensor of each inclusion phase $\boldsymbol{S}_{i}^{m}$ and the Eshelby tensor of its corresponding matrix-inclusion cell. Fig. 4 illustrates how the $\boldsymbol{S}_{i}^{m}$ and $\boldsymbol{S}_{\mathrm{D}i}^{m}$ are determined for the proposed model, where the stack bonded pattern is used as an example for simplicity. For each type-i inclusion, the Eshelby tensor $\boldsymbol{S}_{i}^{m}$ is calculated based on its own aspect ratio and the Eshelby tensor $\boldsymbol{S}_{\mathrm{D}i}^{m}$ is calculated based on the aspect ratio of the global RVE ($\Omega_{Di} = \Omega_{RVE}$). This means that different types of inclusions correspond to different aspect ratios, while the aspect ratios of different types of matrix-inclusion cells are chosen to be identical (equal to the aspect ratio of the RVE). Due to the

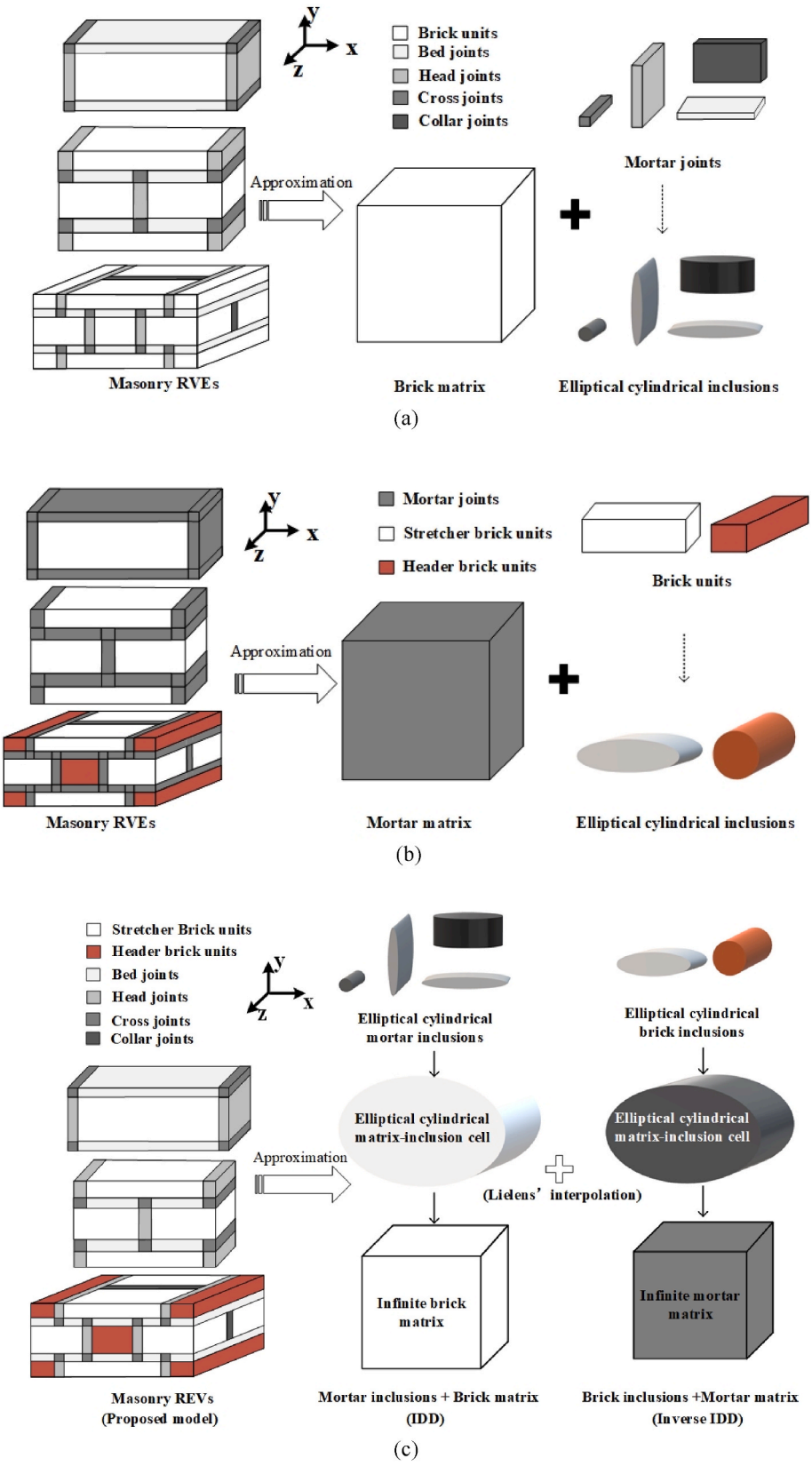

Fig. 3. Assumptions of matrix-inclusion system: (a) elliptical cylindrical mortar inclusions embedded in the brick matrix for classical methods (Pietruszczak and Niu, 1992); (b) elliptical cylindrical brick inclusions embedded in the mortar matrix for classical (inverse) methods (Kumar et al., 2016; Bati et al., 1999; Drougkas and Sarhosis, 2021); (c) matrix-inclusion assumption for the proposed model.

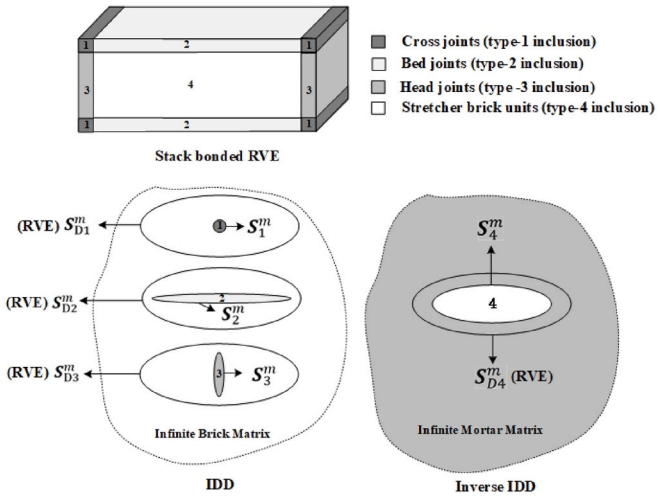

Fig. 4. Schematic illustration for the selection of each type of inclusion and its corresponding matrix-inclusion cell to determine the Eshelby tensors S_i^m and S_{Di}^m for the proposed model (exemplified by stack bonded pattern).

differences in the aspect ratios of inclusions, the Eshelby tensor S_i^m is different from each other's ($S_1^m \neq S_2^m \neq S_3^m \neq S_4^m$ in Fig. 4). It should be noted that the calculation of the Eshelby tensor also depends on the Poisson's ratio of the surrounding matrix besides the aspect ratio values, as shown in Appendix A. Therefore, although all the matrix-inclusion cells have an identical aspect ratio for a given masonry RVE, the Eshelby tensors S_{Di}^m used in the IDD (brick as matrix) and inverse IDD (mortar as matrix) estimates are different when the Poisson's ratios of brick and mortar are different ($S_{D1}^m = S_{D2}^m = S_{D3}^m \neq S_{D4}^m$ in Fig. 4).

6. Model validation against FEM

Experimental data about the Poisson's ratio, out-of-plane Young's moduli and shear moduli of masonry are limited in the literature. Consequently, the proposed model is initially validated through a parametric comparison against the FEA results. The meshes used in the FEA are given in Fig. 5. Similarly to earlier studies (Kumar et al., 2016; Zucchini and Louren ç o, 2002; Drougkas et al., 2015b), twenty-noded quadratic three-dimensional elements with reduced integration are used in the simulation with a maximum element size of 5mm.

Masonry is a two-dimensionally periodic material. The masonry RVE is considered such that the masonry domain can be generated by repeating the RVE in horizontal and vertical directions (Kumar et al., 2016). This implies that each RVE in the composite has the same deformation mode and there is no separation or overlap between the neighboring RVEs. Therefore, periodic boundary conditions (PBC) are applied to the FE models to assure displacement conformity and periodicity at the external faces of the masonry RVE in horizontal and vertical directions.

For a volume of RVE denoted by V, the periodicity conditions on the boundary surface ∂V is defined as (Xia et al., 2003):

$$u_i(x_1, x_2, x_3) = \bar{\varepsilon}_{ik} x_k + u_i^*(x_1, x_2, x_3) \tag{9}$$

where u_i is the displacement components, $\bar{\varepsilon}_{ik}$ is the average strain and u_i^* is the periodic part of the displacement components on the boundary surface ∂V. For parallelepiped RVE models as used in this study, the displacements on a pair of opposite boundary surfaces with normals along direction j (horizontal and vertical directions) are expressed as:

$$u_i^{j+} = \bar{\varepsilon}_{ik} x_k^{j+} + u_i^* \tag{10a}$$

$$u_i^{j-} = \bar{\varepsilon}_{ik} x_k^{j-} + u_i^* \tag{10b}$$

where index "$j+$" means along the positive j direction and "$j-$" means along the negative j direction. The difference between Eqs. (10a) and (10b) is:

$$u_i^{j+} - u_i^{j-} = \bar{\varepsilon}_{ik}\left(x_k^{j+} - x_k^{j-}\right) = \bar{\varepsilon}_{ik} \Delta x_k^j = constant \tag{11}$$

For the parallelepiped RVE models, Δx_k^j is constant. This means that the PBC can be described as keeping constant the displacement difference of two pairs of nodes on the opposite boundary surfaces.

In present study, PBCs are imposed with adequate tying of the displacements of the nodes on opposite surfaces of the FE models in horizontal and vertical directions, as shown in Fig. 6. Specifying three reference nodes (p_1, p_2 and p_3), PBCs are achieved by linking the degrees of freedom (DoF) of the nodes on two pairs of opposite surfaces to those of the reference nodes (Omairey et al., 2019):

$$u_{x(top\ nodes)} - u_{x(bottom\ nodes)} = u_{xp1} - u_{xp2} \tag{12a}$$

$$u_{y(top\ nodes)} - u_{y(bottom\ nodes)} = u_{yp1} - u_{yp2} \tag{12b}$$

$$u_{z(top\ nodes)} - u_{z(bottom\ nodes)} = u_{zp1} - u_{zp2} \tag{12c}$$

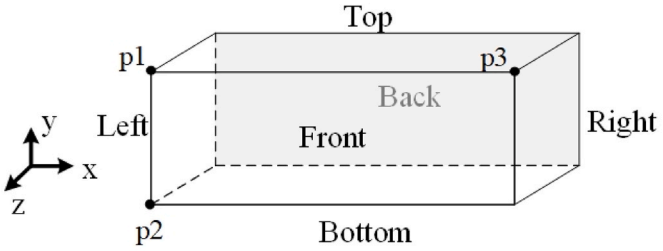

Fig. 6. The reference nodes and the boundary surfaces in FE models for the definition of periodic boundary conditions.

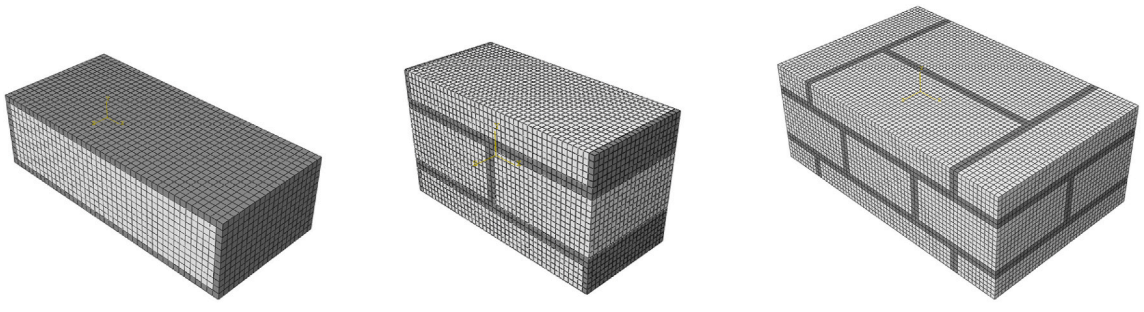

Fig. 5. FE models of masonry RVEs: (a) stack bonded, (b) running bonded and (c) Flemish bonded.

$$u_{x(\text{left nodes})} - u_{x(\text{right nodes})} = u_{xp1} - u_{xp3} \tag{12d}$$

$$u_{y(\text{left nodes})} - u_{y(\text{right nodes})} = u_{yp1} - u_{yp3} \tag{12e}$$

$$u_{z(\text{left nodes})} - u_{z(\text{right nodes})} = u_{zp1} - u_{zp3} \tag{12f}$$

where u_x, u_y andu_z are displacement components along x, y and z directions, respectively. Refer to Fig. 6 to identify Left-Right, Top-Bottom and Front-Back surfaces along with x, y and z directions, respectively. It should be noted that, in Eq. (12a-f), the nodes in a pair of opposite surfaces should have one-to-one correspondence. No constraint is imposed in z direction and the front and back surfaces remain free to deformation for both applied normal and shear stresses, as there is no periodicity in that direction.

Stress-prescribed analyses have been carried out in present study, with uniform normal stresses (pressure) and shear stresses (surface traction) being applied on the surfaces of the FE models. The resulting stress distribution in the constituents of the masonry composite is not uniform but rather depends on the relative elasticity parameters of the involved components. The effective elastic constants of masonry are obtained by six loading conditions of the RVE under compression along x, y and z axes, and shear in xy, xz and yz planes. For each loading condition, the average stresses and strains in the RVE are calculated as (Yang et al., 2012):

$$\overline{\sigma}_{ij} = \frac{1}{V}\int_V \sigma_{ij} dV = \sum_{e=1}^{n} \frac{\sigma_{ij}^{(e)}}{n} = \Sigma_{ij} \tag{13a}$$

$$\overline{\varepsilon}_{ij} = \frac{1}{V}\int_V \varepsilon_{ij} dV = \sum_{e=1}^{n} \frac{\varepsilon_{ij}^{(e)}}{n} \tag{13b}$$

where $\overline{\sigma}_{ij}$ and $\overline{\varepsilon}_{ij}$ are the average stresses and strains in the RVE, respectively. V is the volume of the RVE. n is the number of elements in the FE model. $\sigma_{ij}^{(e)}$ and $\varepsilon_{ij}^{(e)}$ are the average stresses and strains for a generic element. $\Sigma_{ij}$is the prescribed stresses (uniform pressure or surface traction) on the surfaces of the FE model. It should be mentioned that the above equations are only valid in the case all the elements of the mesh of the RVE share the same volume, which is the case in this study. After obtaining $\overline{\sigma}_{ij}$ and $\overline{\varepsilon}_{ij}$, the effective compliance tensor D^*_{ijkl} of a masonry RVE can be obtained from Eq. (14) (Xia et al., 2003). The effective elastic constants of masonry RVE can be derived from D^*_{ijkl} accordingly.

$$\overline{\sigma}_{ij} = D^*_{ijkl}\overline{\varepsilon}_{kl} \tag{14}$$

In this study, the mortar joints and bricks are all considered isotropic and the global orthotropic response of the homogenized masonry is caused by the geometrical arrangement of the constituents. To make a comparison with other classical micromechanical models, the parameters of the masonry constituents used in earlier work (Zucchini and Louren ç o, 2002; Drougkas et al., 2015b) are adopted in this section. The dimensions of bricks are $210 \times 52 \times 100\text{mm}^3$ ($l_b \times h_b \times t_b$), and a value of 10mm is adopted for the thickness of mortar joints ($l_m = h_m = t_m = 10\text{mm}$). The Young's modulus and Poisson's ratio of bricks are 20 GPa ($E_b = 20$ GPa) and 0.15 ($\nu_b = 0.15$), respectively. The Poisson's ratio of mortar is 0.15 ($\nu_m = 0.15$). The Young's modulus of mortar is changed to yield varied values for brick-to-mortar stiffness ratio from 1 to 1000 ($1 \le E_b/E_m \le 1000$). Different stiffness ratios between mortar and bricks are considered. This allows to assess the performance of each mean-field homogenization models for inelastic behavior. As stated by Zucchini & Lourenço (Zucchini and Lourenço, 2002), nonlinear behavior is associated with (tangent) stiffness degradation and homogenization of nonlinear process will result in large stiffness differences between the components. Note that the ratio E_b/E_m tends to infinity when softening of the mortar is complete and only the unit remains structurally active.

6.1. Stack and running bonded masonry

Fig. 7 and Fig. 8 show the prediction results of effective vertical Young's moduli E^*_y from different mean-field homogenization models in the range $1 \le E_b/E_m \le 1000$ for stack and running bonded patterns, respectively. Except the Voigt, Reuss and dilute models that ignore the interactions between phases, all other homogenization models can provide relatively precise predictions for the vertical Young's moduli E^*_y in the range $1 \le E_b/E_m \le 10$. This is consistent with the results in literatures (Kumar et al., 2016; Bati et al., 1999; Wang et al., 2007). However, with increasing the stiffness ratios E_b/E_m from 10 to 1000, unacceptable errors are found for these classical models. For large stiffness ratios, compared with the FE results, the models assuming mortar joints as inclusions all overestimate the vertical effective Young's moduli E^*_y. On the contrary, almost all the inverse models underestimate the effective elastic properties. The only exception is the SCS scheme for which the values predicted by the SCS and the inverse SCS models are both significantly higher than the FE results, which confirms the claim that the SCS method is suitable for the prediction of polycrystals, but not for two-phase materials (Pierard et al., 2004).

For the dimensions and properties of masonry constituents adopted in this section, errors of the models with mortar joints as inclusions are much larger than those of the inverse models with bricks as inclusions when the stiffness ratios E_b/E_m are higher than 10. This might be attributed to the fact that the models considering mortar joints as three separated inclusion families fail to evaluate the interactions between the mortar inclusions, which are connected with each other in real masonry. In this respect, for the models with mortar as inclusions, two other possible choices for the discretization of mortar joints excluding the cross joints are considered here: i). Continuous horizontal mortar joints (Fig. 9a) and ii). Continuous vertical mortar joints (Fig. 9b). Fig. 10 shows the comparison between the three possible choices of the discretization of mortar joints for the prediction of E^*_y for a stiffness ratio $E_b/E_m = 30$. For the stack bonded masonry, the three kinds of discretization provide nearly equal prediction results for all the models with mortar as inclusions. This can be explained by the fact that the cross joints are located in the corners of the stack bonded RVE, thus with minor influence on the overall continuity of mortar joints in both horizontal and vertical directions, i.e., the aspect ratios of horizontal (or vertical) mortar joints show little difference under the three kinds of discretization assumptions. For the running bonded masonry, the model with continuous horizontal mortar joints results in lower values of E^*_y with respect to the model with cross joints, but still provide a large overestimation with respect to the FEM results. The continuous horizontal mortar joints can better reveal the interactions between the mortar inclusions in the horizontal direction. Nevertheless, the different kinds of discretization of mortar joints have almost no influence on the D-I and the proposed models, because the contribution of the MT and IDD schemes to the Lielens' interpolative function is limited (see Eq. (6)).

The discretization choice of continuous horizontal mortar joints is adopted in the following analysis. Results of all the orthotropic effective elastic constants predicted by different models are summarized in Tables 2 and 3, providing the average and maximum absolute errors with respect to the FE benchmark in the range $1 \le E_b/E_m \le 1000$. It should be noted that all models can make accurate predictions for the transversal Young's modulus E^*_z in the entire range of stiffness ratios E_b/E_m. This can be attributed to the fact that the stack and running bonded masonry are both single-leaf structures without change in geometry across the thickness of the RVE, thus the use of elliptical cylindrical inclusions is reasonable. In such case, E^*_z is less influenced by the properties of the mortar because the tension in this direction acts mainly on the stiffer phase, namely the bricks (Almeida and Louren ç o, 2020; Drougkas et al., 2015b). In the mean-field homogenization models, an inclusion with lower stiffness (i.e., the mortar) will result in the amplification of shear

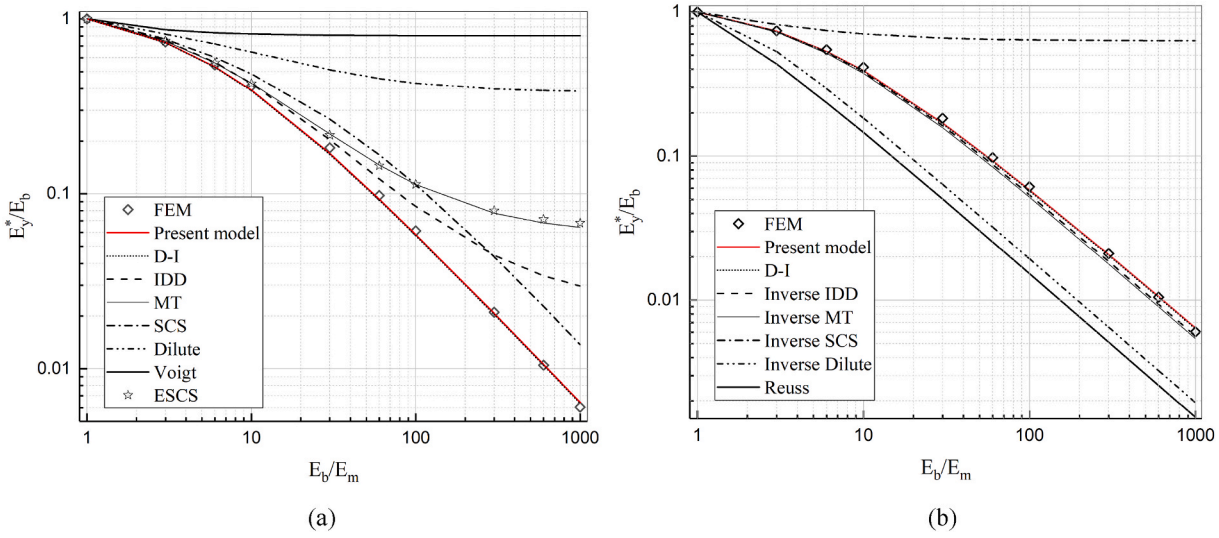

Fig. 7. The macroscopic vertical Young's moduli E_y^* calculated by different mean-field homogenization models for stack bonded pattern: (a) the models with mortar joints as inclusions; (b) the inverse models with bricks as inclusions.

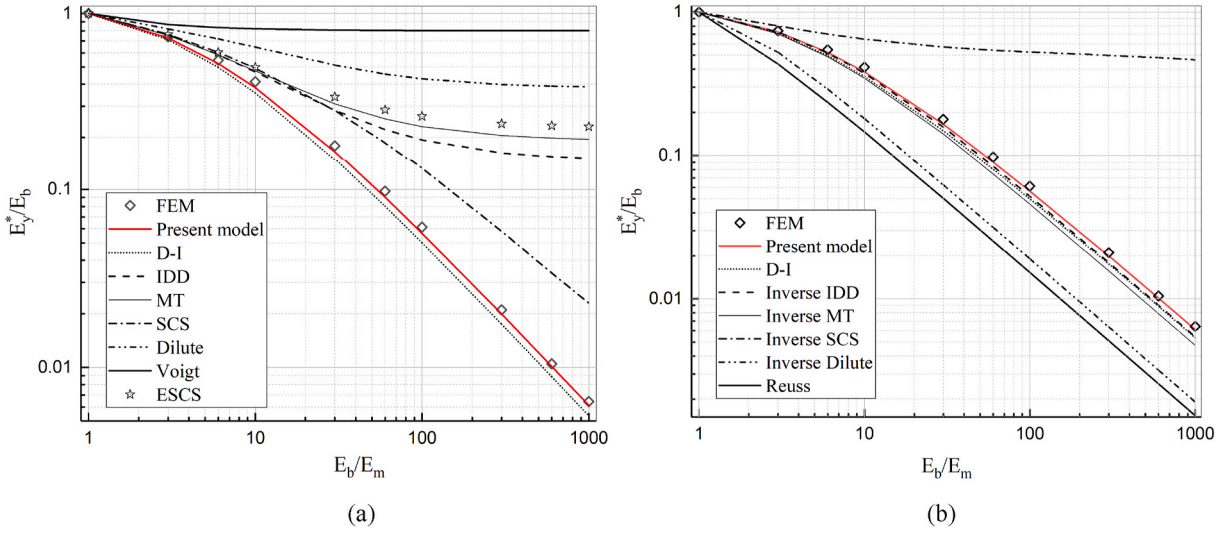

Fig. 8. The macroscopic vertical Young's moduli E_y^* calculated by different mean-field homogenization models for running bonded pattern: (a) the models with mortar as inclusions; (b) the inverse models with bricks as inclusions.

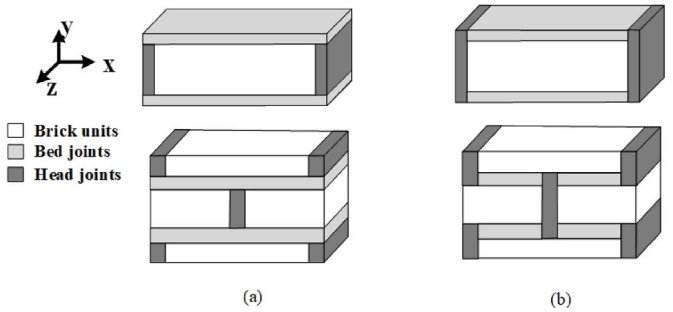

Fig. 9. Alternative choices for the discretization of mortar joints: (a) continuous horizontal mortar joints; (b) continuous vertical mortar joints.

and normal strain under a given macro stress, and the degree of such amplification effect is governed by the Eshelby tensor (Dormieux et al., 2006). The components S_{3333}, S_{3322} and S_{3311} of the Eshelby tensor for elliptic cylindrical inclusions are zeros, as shown in Appendix A. Accordingly, the influence of such amplification effect on the normal strain in the z direction may be very limited, resulting in a lower degree of dependency of E_z^* on the properties of mortar. The same explanation applies to the assumption of brick inclusions, as a stiffer inclusion is responsible for the shear and normal strain reduction under a given macro stress.

Although with relevant errors, the D-I model shows the best performance among the classical mean-field homogenization schemes. This is consistent with the conclusion in (Pierard et al., 2004), where the authors compared different well-known mean-field homogenization models for composite fibers and concluded that "The interpolative double inclusion model proposed by Lielens provides perhaps the best mean-field predictions to date for two-phase composites". However, see Table 2, the D-I model shows unacceptable errors up to 22.9% and 33.4% for the predictions of E_x^* and ν_{xy}^*, respectively, for the stack bonded pattern.

The proposed model outperforms the classical mean-field homogenization models and makes accurate predictions for all the orthotropic

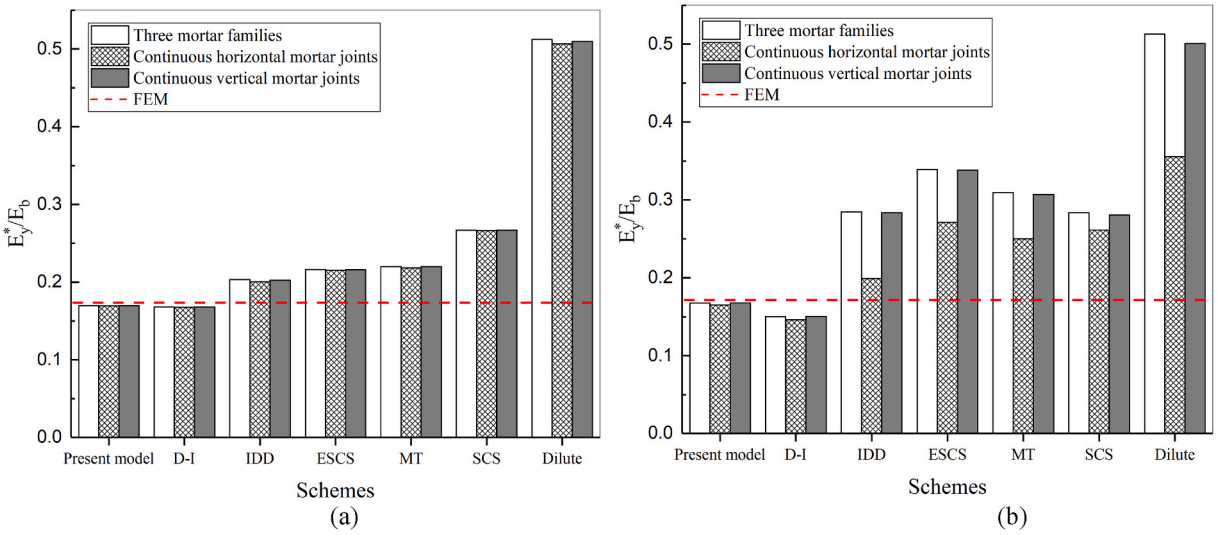

Fig. 10. Comparison between the three possible choices of the discretization of mortar joints for the prediction of E_y^* for a stiffness ratio $E_b/E_m = 30$: (a) stack bonded; (b) running bonded.

elastic constants for both stack and running bonded patterns. Fig. 11 and Fig. 12 present the orthotropic elastic constants predicted by the proposed model for different stiffness ratios E_b/E_m for stack and running bonded masonry, respectively. It is observed that the values obtained with the FE method and the proposed model are very close for the entire range of stiffness ratios, with differences being mainly restricted to the in-plane Poisson's ratio, v_{xy}^*. In the stack bonded case, the transversal Young's modulus is larger than its counterparts in the other two directions. The vertical and horizontal Young's moduli are significantly decreased with the decline in the stiffness of mortar, while the Young's modulus in transversal direction is less influenced by the properties of mortar, with a tendency to practically stabilize from E_b/E_m values higher than 10. Moreover, the vertical Young's modulus is a little bit lower than the horizontal one and the same tendency is observed in the experimental tests by other researchers (Ma et al., 2001; Nasedkina and Rajagopal, 2017), which can be attributed to the fact that the mortar phase in horizontal direction has a lower volume fraction than the vertical one (Stefanou et al., 2008). The horizontal Young's modulus of the running bonded case is higher than that of stack bonded pattern because of the staggered arrangements of the bed joints in horizontal direction, as also reported by (Drougkas et al., 2015b), while the transversal and vertical Young's moduli for running bonded pattern are almost the same as for the stack bonded.

The proposed model is also compared with the well-known single-step analytical micromechanical models by Zucchini & Lourenço (Zucchini and Louren ç o, 2002) and Drougkas et al. (2015b), where the authors derived the average elasticity of masonry by assembling the stress equilibrium and strain compatibility conditions in the RVE into an collection of equations which can be analytically solved. The Zucchini & Lourenço model only addressed the running bonded case, while Drougkas et al. developed models for both the stack, running and Flemish bonded typologies. For the stack bonded pattern, the proposed model provides a more accurate prediction for the in-plane Poisson's ratio v_{xy}^* than the one of Drougkas, while errors of these two models are nearly equal for other orthotropic elastic constants (Fig. 11). For the running bonded pattern, the errors of the proposed model are slightly higher for the predictions of v_{xy}^*, while the proposed model provides nearly equal or even more accurate predictions than the two reference models for other elastic constants (Fig. 12). Additionally, the proposed model has some distinct advantages over such analytical micromechanical models. The proposed model can be easily applied to various masonry patterns by selecting different masonry RVEs, while the development of the models of Zucchini & Lourenço and Drougkas et al. depends on the masonry patterns (i.e., each pattern corresponds to a different set of expressions). Furthermore, the proposed model has advantages in nonlinear extension. Many multiscale methods have been established over the past decades for the nonlinear analyses of various composite-like materials, such as metal composites (Doghri et al., 2016), alloys (Pardoen and Hutchinson, 2003), rocks (Deude et al., 2002; Pens é e et al., 2002), cementitious materials (Pichler et al., 2007; Ulm et al., 2004), geomaterials (Zhu et al., 2009) and bones (Fritsch et al., 2013; Morin et al., 2017), by combining the mean-field homogenization technique with different damage, plasticity or fracture models at macroscopic and microscopic scales. The proposed model has the potential to be applied to these well-established mean-field homogenization based multiscale methods to achieve the nonlinear analysis of masonry. For example, by following the so-called microporomechnics theory (Dormieux et al., 2006) and further considering the microcracks as several families of penny-shaped inclusions, the macroscopic nonlinear response of homogenized masonry can be derived as a result of the evolution of open microcracks, the frictional sliding on the lips of closed microcracks and the opening-closure transition between microcracks. A preliminary model is presented in (Zhou et al., 2022).

6.2. *Flemish bonded masonry*

As discussed above, the assumption of elliptical cylindrical inclusions provides a good approximation for the deformation characteristics of the single-leaf structures in the wall thickness direction; nevertheless, this assumption is not suitable for the double-leaf Flemish bonded masonry due to the existence of collar joints (Fig. 1c). Therefore, for the Flemish bonded case, three assumptions are made for the inclusion shapes: i). A model in which every inclusion is considered as an elliptic cylinder, ii). A model in which every inclusion is considered as an ellipsoid, iii). A model in which a combination of elliptical cylindrical and ellipsoidal inclusions is considered. Specifically, for the third model, the bed, head and cross mortar joints and the header bricks with unchanging geometry in the z direction are approximated by the elliptical cylinders, while the collar joints and stretcher bricks with non-continuous layout across the thickness are approximated by ellipsoids (Fig. 13). It should be noted that, for the proposed model, each inclusion and corresponding matrix-inclusion cell (RVE) should be idealized as the same type to ensure the rationality of the results. Specifically, the matrix-inclusion cell is idealized as an elliptical cylinder for the elliptical cylindrical inclusions and the matrix-inclusion cell is idealized as an

Table 2
Mean and maximum absolute errors (%) of the orthotropic elastic constants predicted by different homogenization models in the range $1 \leq E_b/E_m \leq 1000$for stack bonded.

Model name	E_x^*		E_y^*		E_z^*		G_{xy}^*		G_{xz}^*		G_{yz}^*		ν_{xy}^*		ν_{xz}^*		ν_{yz}^*	
	Mean	Max.	Mean	Max.	Mean	Max.	Mean	Max.	Mean	Max.	Mean	Max.	Mean	Max.	Mean	Max.	Mean	Max.
Present model	3.8	6.6	1.9	6.4	1.2	4.8	3.9	8.0	3.8	7.6	2.1	7.6	5.5	13.7	1.9	3.0	3.0	7.9
D-I	13.8	22.9	2.9	8.3	1.0	4.5	9.8	11.9	11.3	22.2	5.0	12.5	18.6	33.4	1.9	3.0	4.7	12.5
Inverse MT	18.5	31.6	10.0	15.4	1.0	4.5	19.3	36.9	4.8	8.1	1.5	3.8	17.8	35.4	18.8	32.5	7.2	18.0
Inverse IDD	9.1	15.7	7.5	12.0	1.0	4.5	14.3	21.9	5.9	9.7	4.2	10.6	10.3	24.7	9.5	19.7	5.9	15.0
Inverse Dilute	58.5	82.2	53.7	69.2	1.0	4.5	56.9	73.8	49.9	74.0	51.7	67.0	233.5	511.9	58.6	82.5	53.0	69.7
Inverse SCS	597.9	2901.2	1781.6	8755.6	11.2	16.3	1457.	6827.2	664.5	3229.3	1839.7	8827.1	150.3	354.3	795.9	3733.1	2613.3	13,664.2
MT	417.7	2039.9	194.4	966.5	0.9	4.4	296.7	1471.4	592.0	2877.5	365.5	1766.9	110.0	287.9	418.9	2009.6	207.2	1099.8
IDD	258.5	1365.2	81.1	393.0	1.7	5.1	301.2	1489.8	601.7	2920.5	370.0	1785.8	107.7	283.5	422.9	2026.6	207.5	1100.9
SCS	339.1	1495.2	58.4	116.8	2.7	11.1	43.1	101.1	628.3	3044.0	85.2	194.3	1442.7	6295.6	39.7	272.9	939.3	4640.0
Dilute	21.8	80.4	1295.4	6302.1	1.0	4.5	1329.5	6591.5	401.9	1976.2	1779.0	9023.4	129.9	303.6	22.3	80.7	151.5	2421.7
ESCS	253.8	1275.9	204	1027.1	1.0	4.5	305.2	1539.3	443.6	2180.8	364.9	1783.4	171.0	479.2	240.8	1195.1	192.9	1048.9
Voigt	775.1	3704.4	2687	13,184.3	1.0	4.5	2213.8	10,485.7	849.5	4075.3	2767.1	13,257.2	102.1	245.5	777.3	3650.7	2839.0	14,844.7
Reuss	52.2	76.3	61.0	74.7	14.5	21.4	50.1	74.0	11.8	18.0	67.2	99.4	102.1	245.5	777.3	3650.7	2839.0	14,844.7

Table 3
Mean and maximum absolute errors (%) of the orthotropic elastic constants predicted by different homogenization models in the range $1 \leq E_b/E_m \leq 1000$for running bonded.

Model name	E_x^*		E_y^*		E_z^*		G_{xy}^*		G_{xz}^*		G_{yz}^*		ν_{xy}^*		ν_{xz}^*		ν_{yz}^*	
	Mean	Max.	Mean	Max.	Mean	Max.	Mean	Max.	Mean	Max.	Mean	Max.	Mean	Max.	Mean	Max.	Mean	Max.
Present model	1.9	3.9	4.9	7.6	0.6	1.2	3.9	8.4	3.7	7.3	0.9	3.8	4.9	10.6	1.9	7.5	4.1	8.9
D-I	2.4	4.4	12.8	18.3	0.7	1.3	3.0	6.5	6.5	13.7	0.7	3.3	5.4	12.3	2.2	3.9	3.9	7.8
Inverse MT	6.9	14.0	17.8	26.3	0.7	1.3	8.2	11.7	1.7	3.9	6.1	9.9	7.8	19.4	4.8	9.9	8.6	17.2
Inverse IDD	5.2	10.9	10.2	15.7	0.7	1.3	8.4	12.0	3.	5.4	6.4	10.3	7.3	15.7	3.1	9.7	9.2	20.5
Inverse Dilute	53.0	79.5	54.3	70.3	0.7	1.3	54.3	69.2	47.8	77.2	53.3	68.5	164.3	359.0	52.0	78.5	53.8	70.5
Inverse SCS	458.8	2230.2	1542.5	7132	12.6	17.5	1721.4	8266.4	352.4	1707.7	1764.0	8452.2	92.2	220.4	641.3	3049.5	2546.5	12,943.8
MT	252.7	1407.6	612.8	2936	0.7	1.3	370.2	1822.6	288.4	1415.6	366.0	1768.7	58.0	163.3	298.4	1479.8	202.9	1044.5
IDD	314.1	1546.7	474	2266	0.3	1.2	379.0	1859.9	310.7	1511.9	370.0	1785.8	64.5	179.3	327.4	1610.0	202.9	1044.5
SCS	241.2	1077.1	95.4	257.8	5.3	14.5	54.6	124.2	319.7	1553.1	72.7	162.1	1081.0	4715.1	49.6	913.0	910.8	4361.3
Dilute	29.5	85.2	1256	5903.4	0.7	1.3	16,143.1	81,240.4	198.8	1008.0	17,790.2	90,234.6	81.7	194.0	28.2	84.5	123.5	2303.1
ESCS	181.4	940.8	727	3477.7	0.7	1.3	384.2	1908.7	221.9	117.2	365.0	1783.4	143.2	376.2	181.6	941.4	188.4	995.0
Voigt	582.3	2777.9	2606.0	12,357.5	0.7	1.3	2697.9	12,950.7	450.1	2128.3	2767.1	13,257.3	60.8	151.6	611.4	2915.8	2781.9	14,141.3
Reuss	55.7	82.1	61.1	76	13.4	20.3	14.0	19.8	57.8	86.1	11.8	17.9	60.8	151.6	611.4	2915.8	2781.9	14,141.3

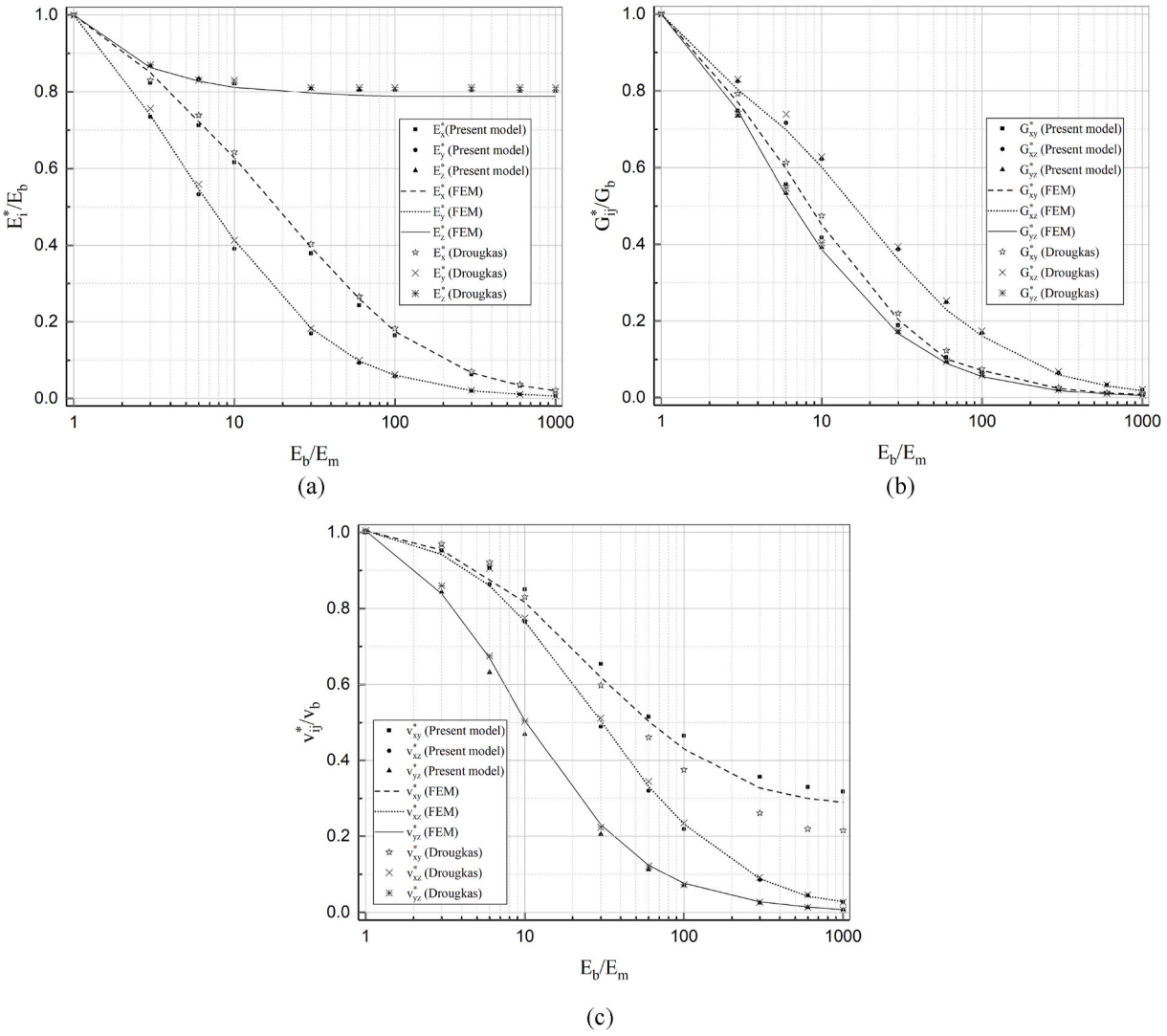

Fig. 11. Comparison between the proposed model, the FEA and the reference micromechanical model for stack bonded pattern: (a)Young's moduli; (b) Shear moduli; (c) Poisson's ratios.

ellipsoid for the ellipsoidal inclusions, as shown in Fig. 13. Appendix B gives the expression of Eshelby tensor for ellipsoidal inclusions. Fig. 14 shows the comparison between the three models with different assumptions for the inclusions' shape, providing the errors with respect to the FEA results for $1 \leq E_b/E_m \leq 1000$. The first model with elliptical cylindrical inclusions shows a relatively smaller error for the prediction of E_x^*. Among the three assumptions, the third one with the combination of elliptical cylinders and ellipsoids provides the best approximation for the remaining elastic constants.

Fig. 15 shows the orthotropic elastic properties predicted by the proposed model in the range $1 \leq E_b/E_m \leq 1000$ for the Flemish bonded pattern, including a comparison with the FE analysis, the micromechanical model by Drougkas et al. (2015b) and the D-I model. Compared with the stack and running bonded pattern, the transversal Young's modulus E_z^* of Flemish bonded case is significantly reduced due to the existence of collar joints. Compared with the D-I model that shows the best performance among the classical mean-field models, the proposed model makes better prediction results which are much closer to the FEA values. Due to the lack of considering the inclusion distributions in the masonry RVE, the classical mean-field homogenization schemes result in large errors for the effective stiffness tensor of Flemish bonded masonry. It can be observed that, even in the range $1 \leq E_b/E_m \leq 10$, the D-I model which shows the best performance among the classical mean-field models still results in large errors for the prediction of E_z^*, E_y^*, G_{xz}^* and v_{yz}^*. Compared with the FEA results, the in-plane Poisson's ratio v_{xy}^* is slightly overestimated by the proposed model. Large differences exist between the proposed model and FE benchmark for the prediction of out-of-plane Young's moduli E_z^* when the stiffness ratio E_b/E_m is larger than 30. However, the proposed model makes accurate prediction results for the remaining elastic constants, especially for the shear moduli.

7. Model validation against experiments

An analysis of case studies is performed to further examine the feasibility and accuracy of the proposed model. After an extensive literature review on the research of masonry compression tests, the proposed model has been applied to a large number of experimental cases. In many of the cases, the values of Young's moduli and/or Poisson's ratios of the constituents are not given. Accordingly, only the experimental cases that provide the values of Young's moduli of masonry constituents are selected. For the cited work lacking the values of Poisson's ratios of mortar joints, a nominal value is used according to the type of mortar. The selection of such nominal values should be based on the mortar's deformability, i.e., lower values of Poisson's ratios should be chosen for stronger mortar and vice versa. Following the work in (Drougkas et al., 2015b), the nominal values of 0.25, 0.20 and 0.15 are

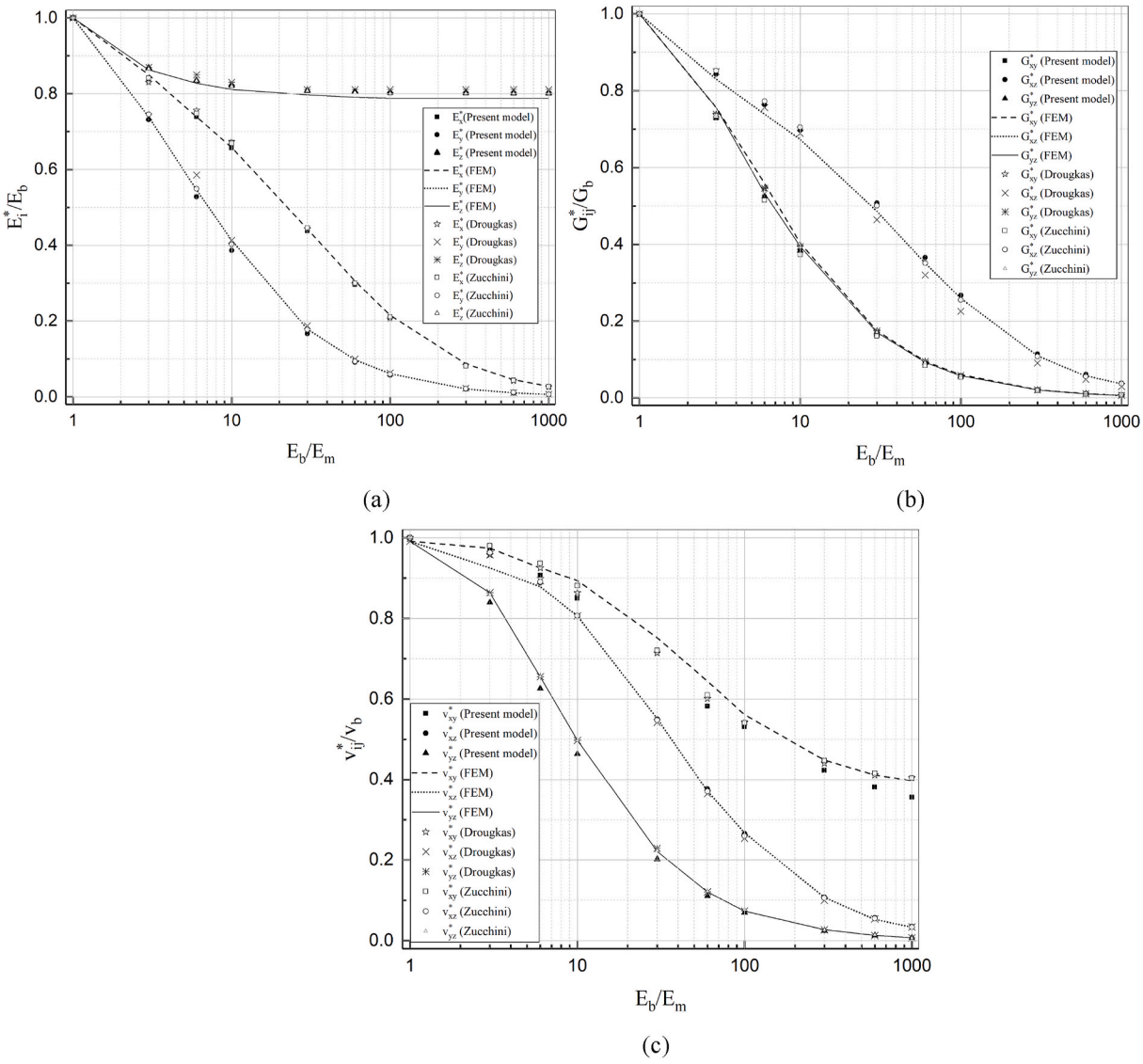

Fig. 12. Comparison between the proposed model, the FEA and the reference micromechanical models for running bonded pattern: (a)Young's moduli; (b) Shear moduli; (c) Poisson's ratios.

adopted in this study for the lime mortar (weak) (Drougkas et al., 2016, 2019; Kaushik et al., 2007; Panizza et al., 2012), lime-cement mortar (intermediate) (Kaushik et al., 2007; Page, 1978; Drougkas et al., 2019; Gumaste et al., 2007; Venkatarama Reddy and Gupta, 2006; Vermeltfoort et al., 2007) and Portland cement mortar (strong) (Kaushik et al., 2007; Drougkas et al., 2019; Ferretti et al., 2015; Oliveira et al., 2006), respectively. The selected experimental cases represent a great variety of types, properties and dimensions of the masonry constituents. The selected cases consist of the stack, running and Flemish bonded masonry patterns. Besides solid clay bricks (SC) that represents the most common unit material, soil-cement blocks (S-CB), stabilized mud blocks (SMB), calcium silicate bricks (CS), autoclaved aerated concrete blocks (AAC), and solid softmud bricks (SSM) are considered.

Table 4 summarizes the results of case studies for the effective vertical Young's modulus, where the prediction from the proposed model is compared with the FEA results and experimental values. The prediction results from the proposed model agree well with the FEM values for the three selected masonry patterns (Fig. 16a). However, larger differences exist between the model results and corresponding experimental values in a few cases (Fig. 16b). In this respect, the potential factors including the mortar type, brick type and the stiffness ratios, which may lead to these differences, are further analyzed. Fig. 17 shows the influence of the stiffness ratio of masonry constituents on the errors between results of the proposed model and experimental values. The errors are randomly scattered over the stiffness ratios, indicating that the stiffness ratio has little effect on the performance of the proposed model. The percentages of errors larger than 10% for the different types of mortar and units are shown in Fig. 18. Considering the mortar types, the proposed model gives a prediction closer to the experiments for the lime (weak) and lime-cement (intermediate) mortar. For the types of units, the errors are always lower than 10% for nearly all the cases involving the S-CB, SMB, CS and ACC units, with large errors being restricted to the SC and SSM units. However, the vast majority of available experimental cases in existing literature are limited to lime-cement mortar and SC bricks. Therefore, the conclusion about the effects of constituent types on the performance of the proposed model should be further investigated by experimental programs. Another possible explanation for the differences between experimental values and the results obtained by FEA and the proposed model is as follows: ideal conditions (e.g., perfect materials and perfect interfacial bonds) are considered in the FEA and in the proposed model, while the experiments are generally also influenced by other uncertain factors, such as the manufacturing quality of the

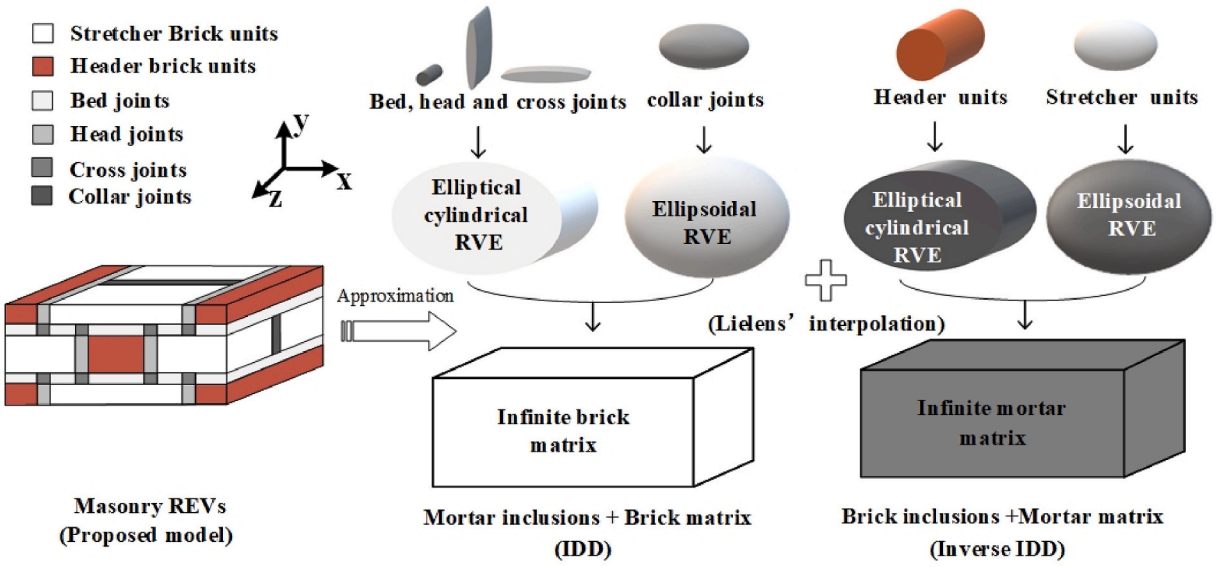

Fig. 13. Assumptions of matrix-inclusion system for Flemish bonded pattern when a combination of elliptical cylindrical and ellipsoidal inclusions is considered.

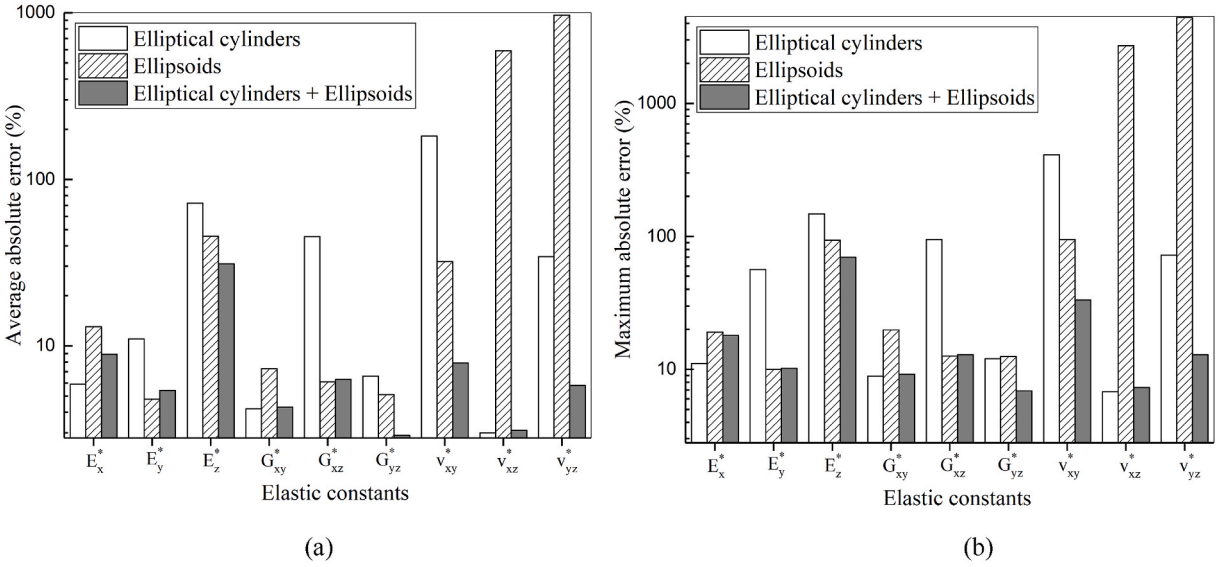

Fig. 14. Average and maximum absolute errors of the proposed model for Flemish bonded masonry in comparison with FEA results in the range $1 \leq E_b/E_m \leq 1000$ considering three possible assumptions for the inclusions' shape: (a) average absolute error; (b) maximum absolute error.

specimens, defects in the material and imperfect bond between the constituents. Accordingly, the FEA and the proposed model are likely to overestimate experimental values.

8. Conclusions

Unreinforced brick masonry, composed of mortar joints and bricks, is considered as an inhomogeneous and orthotropic material that is difficult to characterize. Aiming at developing an analytical-based multi-scale model for masonry, this study represents a first step in which the orthotropic elastic properties of masonry is derived from the isotropic properties of its constituents by applying the mean-field homogenization technique. After comparing the accuracy of various classical mean-field homogenization schemes, an improved model is proposed by combining the advantages of the interaction direct derivative (IDD) and double inclusion (D-I) schemes. The proposed model is able to approximate the distribution of each inclusion in the RVE to some extent by simultaneously considering the geometries of all the microscopic phases and the macroscopic RVE. The results show that the proposed model can provide accurate evaluation for the orthotropic stiffness tensors of different masonry typologies for a wide range of stiffness ratios between brick and mortar, ranging from 1 to 1000, with a simple closed-form solution. The paper itself does not concentrate on the issue of nonlinear homogenization. But as the accuracy of the proposed model is assessed for an increasing ratio between the stiffness of the two components, the benefits of adopting the proposed method for nonlinear analysis are demonstrated. The main results are as follows:

1. Eight classical mean-field homogenization schemes have been applied to the representative element volumes (RVE) of stack, running and Flemish bonded masonry. For each scheme, two assumptions of the matrix-inclusion system were considered, with the bricks or the mortar joints being approximated by elliptical cylindrical inclusions. A wide range of stiffness ratios between brick and mortar, ranging from 1 to 1000, is considered to assess the performance of each homogenization scheme for inelastic behavior. The

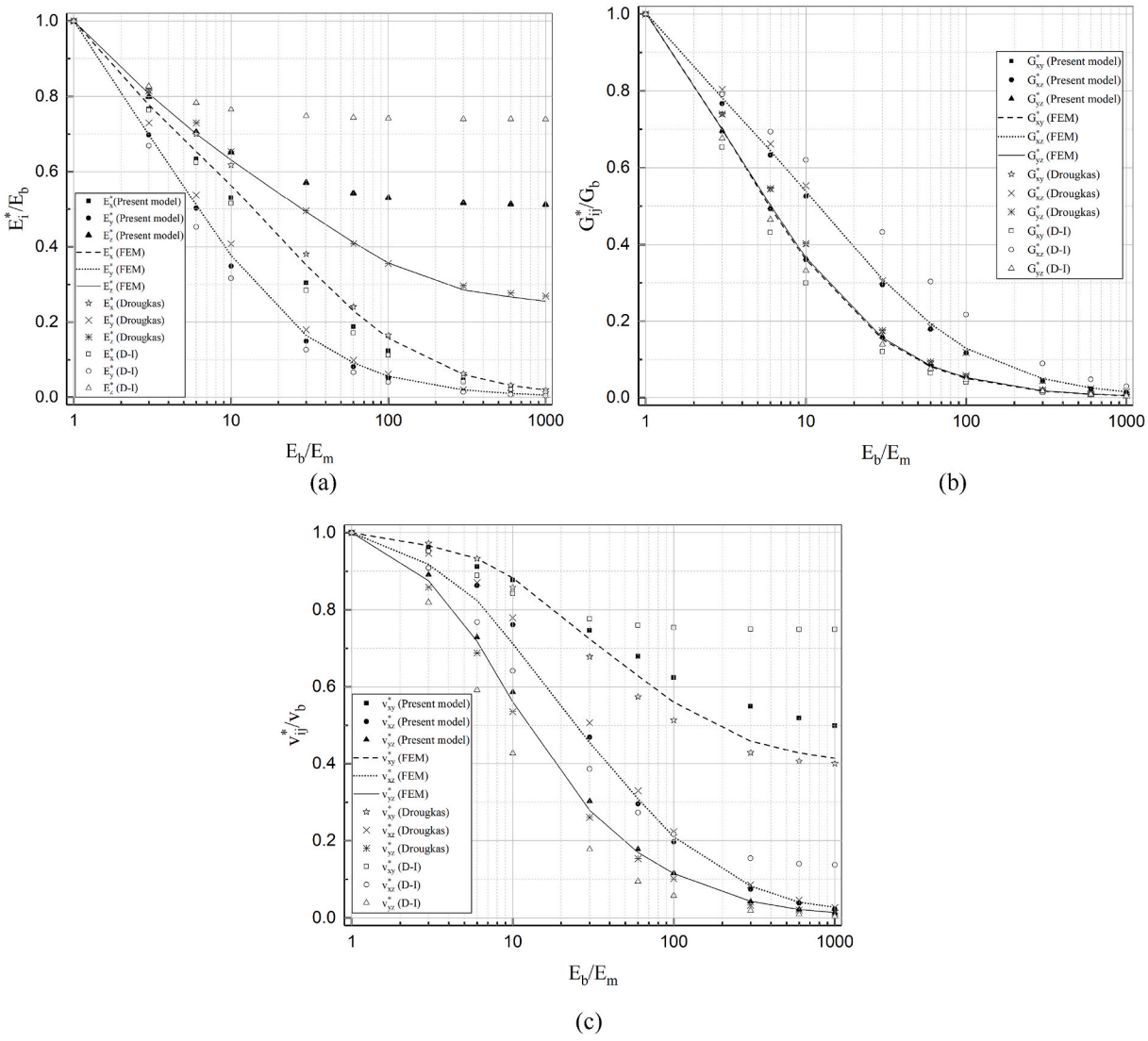

Fig. 15. Comparison between the proposed model, the FEA, the micromechanical model of Drougkas and the D-I model for Flemish bonded pattern: (a)Young's moduli; (b) Shear moduli; (c) Poisson's ratios.

orthotropic elastic constants calculated by these schemes were then compared with those obtained via finite element analyses (FEA). The results show that, among the classical mean-field homogenization schemes, the D-I model shows the best performance but still results in unacceptable errors for the stack bonded masonry, with maximum absolute errors up to 22.9% and 33.4% for the overall horizontal Young's modulus and in-plane Poisson's ratio, respectively.

2. By properly choosing an interpolation between the IDD and the inverse IDD models, a new homogenization model is proposed. The IDD and the inverse IDD methods correspond to the assumptions with mortar joints and bricks, respectively, as inclusion phases. The proposed model well overcomes the limitation of the classical mean-field homogenization models and can simultaneously account for the microscopic geometries of constituents and the global geometry of masonry RVE. Performance of the proposed model is superior to that of the classical mean-field models for the homogenization of the three selected masonry patterns, especially when the stiffness ratios between brick and mortar are higher than 10.
3. The proposed model was initially validated through a comparison against FEA. It shows that the proposed model can make an accurate prediction for the orthotropic elastic properties of the stack and running bonded masonry. For the Flemish bonded pattern, errors of the proposed model are mainly restricted to the out-of-plane Young's modulus when the stiffness ratio between the constituents is larger than 30. The proposed model was also validated against the experimental data obtained from literature. The prediction results from the proposed model are close to the experimental data for the majority of the experimental cases.
4. This paper also investigates the influence of different discretization choices of mortar joints and different assumptions for the inclusions' shapes on the model performance. The discretization choice of continuous horizontal mortar joints provides the most accurate prediction for the vertical Young's modulus, although prediction obtained considering continuous vertical mortar joints or the presence of a cross joint provides similar results. The assumption of elliptical cylindrical inclusions provides a good approximation for the deformation characteristics of single-leaf masonry, while the assumption with the combination of elliptical cylinders and ellipsoids is more appropriate for the Flemish bonded pattern due to the existence of collar joints.
5. The proposed model is easier and faster to be applied with respect to finite element analyses or the other analytical micromechanical models. In particular, regarding the latter category it does not require an ad-hoc derivation for each masonry typology. The

Table 4
Case studies: model results in comparison with the FEA and experimental values for the effective vertical Young's modulus E_y^* (nominal values are in brackets).

Numbers/Refs.	Bond type	[a]Unit type	[b]Mortar type	E_b/E_m	Parameters of units					Parameters of mortar					Results of E_y^*		
					l_b (mm)	h_b (mm)	t_b (mm)	ν_b (−)	E_b (MPa)	l_m (mm)	h_m (mm)	t_m (mm)	ν_m (−)	E_m (MPa)	Exp. (MPa)	FEA (MPa)	Model (MPa)
S1 (Reddy et al., 2009)	Stack	S-CB	II	1.21	305	100	143	0.08	8000	6	–	–	0.19	6600	7800	7921	7896
S2 (Reddy et al., 2009)	Stack	S-CB	II	1.21	305	100	143	0.08	8000	12	–	–	0.19	6600	7200	7389	7804
S3 (Reddy et al., 2009)	Stack	S-CB	II	1.21	305	100	143	0.08	8000	20	–	–	0.19	6600	7100	7264	7698
S4 (Reddy et al., 2009)	Stack	S-CB	II	1.21	305	100	143	0.08	8000	30	–	–	0.19	6600	6900	6986	7587
S5 (Drougkas et al., 2016)	Stack	SC	III	16.97	290	50	140	0.16	4243	10	–	–	{0.25}	250	1469	1157	1203
S6 (Drougkas et al., 2016)	Stack	SC	III	33.94	290	50	140	0.16	4243	10	–	–	0.162	125	417	814	806
S7 (Kaushik et al., 2007)	Stack	SC	III	9.72	230	75	110	{0.15}	5300	10	–	–	{0.25}	545	2239	2176	2152
S8 (Kaushik et al., 2007)	Stack	SC	II	1.61	230	75	110	{0.15}	5300	10	–	–	{0.20}	3300	3542	4403	4296
S9 (Kaushik et al., 2007)	Stack	SC	I	1.41	230	75	110	{0.15}	5300	10	–	–	{0.15}	3750	3585	4517	4322
S10 (Kaushik et al., 2007)	Stack	SC	III	13.79	230	75	110	{0.15}	7516	10	–	–	{0.25}	545	2630	3096	2876
S10 (Kaushik et al., 2007)	Stack	SC	II	2.28	230	75	110	{0.15}	7516	10	–	–	{0.20}	3300	4712	5302	5180
S11 (Kaushik et al., 2007)	Stack	SC	I	2.00	230	75	110	{0.15}	7516	10	–	–	{0.15}	3750	5219	5398	5207
S12 (Oliveira et al., 2006)	Stack	SC	I	3.04	285	50	130	0.20	12,750	10	–	–	{0.15}	4200	10,000	9750	9025
S13 (Gumaste et al., 2007)	Stack	SC	II	4.06	228	75	108	{0.15}	976	12	–	–	{0.20}	238	401	709	664
S14 (Gumaste et al., 2007)	Stack	SC	II	0.46	235	75.5	111	{0.15}	3372	12	–	–	{0.20}	7257	3872	3974	3771
S15 (Panizza et al., 2012)	Stack	SC	II	1.05	125	55	120	{0.15}	5756	10	–	–	{0.25}	5487	2132	5681	5719
S16 (Drougkas et al., 2019)	Stack	SC	III	26.77	188	48	88	0.14	2570	10	–	–	{0.25}	96	296	480	454
S17 (Drougkas et al., 2019)	Stack	SC	III	3.37	188	48	88	0.14	2570	10	–	–	{0.25}	762	670	1797	1653
S18 (Drougkas et al., 2019)	Stack	SC	II	10.94	188	48	88	0.14	2570	10	–	–	{0.20}	235	985	964	891
S19 (Drougkas et al., 2019)	Stack	SC	I	0.77	188	48	88	0.14	2570	10	–	–	{0.15}	3325	865	2726	2704
S20 (Venkatarama Reddy and Gupta, 2006)	Stack	SMB	II	4.72	305	100	143	{0.15}	5900	20	–	–	{0.20}	1250	3100	3294	3396
S21 (Venkatarama Reddy and Gupta, 2006)	Stack	SMB	II	1.13	305	100	143	{0.15}	6100	20	–	–	{0.20}	5400	6000	5857	5749
S22 (Venkatarama Reddy and Gupta, 2006)	Stack	SMB	II	3.05	305	100	143	{0.15}	6100	20	–	–	{0.20}	2000	5100	4318	4480
S23 (Venkatarama Reddy and Gupta, 2006)	Stack	SMB	II	1.52	305	100	143	{0.15}	6100	20	–	–	{0.20}	4000	5300	4713	5333
S24 (Adam et al., 2010)	Stack	SC	–	1.17	250	55	110	0.10	2000	10	–	–	0.20	1700	1936	1950	1934
S25 (Vermeltfoort et al., 2007)	Stack	CS	II	7.95	212	53	100	0.15	16,700	13	–	–	0.22	2100	6800	7849	6764
R1 (Gumaste et al., 2007)	Running	SC	II	0.62	230	75	105	{0.15}	3372	12	12	–	{0.20}	5450	5232	3590	3636
R2 (Gumaste et al., 2007)	Running	SC	II	0.47	230	75	105	{0.15}	3372	12	12	–	{0.20}	7083	4824	3954	3764
R3 (Gumaste et al., 2007)	Running	SC	II	0.39	230	75	105	{0.15}	3372	12	12	–	{0.20}	8568	5024	4030	3853
R4 (Gumaste et al., 2007)	Running	SC	II	4.10	230	75	105	{0.15}	976	12	12	–	{0.20}	238	580	717	652
R5 (Gumaste et al., 2007)	Running	SC	II	0.65	230	75	105	{0.15}	976	12	12	–	{0.20}	1500	735	1033	1045
R6 (Gumaste et al., 2007)	Running	SC	II	0.11	230	75	105	{0.15}	976	12	12	–	{0.20}	8568	400	1250	1308
R7 (Vermeltfoort et al., 2007)	Running	SC	II	2.42	206	50	96	0.13	4000	12.5	10	–	{0.20}	1650	3200	3095	3162
R8 (Page, 1978)	Running	SC	II	6.95	110	35	50	0.167	6740	5	5	–	{0.20}	970	3700	3912	3637
R9 (Ferretti et al., 2015)	Running	ACC	I	0.25	250	50	100	{0.15}	1320	1.5	1.5	–	{0.15}	5300	1473	1462	1368
F1 (Binda et al., 1988)	Flemish	SSM	III	4.12	250	55	120	0.09	4865	10	10	10	0.06	1180	1651	3100	2942
F2 (Binda et al., 1988)	Flemish	SSM	II	0.86	250	55	120	0.09	4865	10	10	10	0.09	5650	3833	5000	5036
F3 (Binda et al., 1988)	Flemish	SSM	I	0.27	250	55	120	0.09	4865	10	10	10	0.12	17,760	4567	6390	6280

[a] Unit type: S-CB = Soil-cement blocks; SC = solid clay bricks; SMB = Stabilized mud blocks; CS = Calcium silicate bricks; AAC = Autoclaved aerated concrete blocks; SSM = Solid softmud bricks.
[b] Mortar type: I = Portland cement mortar (strong); II = Lime-cement mortar (intermediate); III = lime mortar (weak).

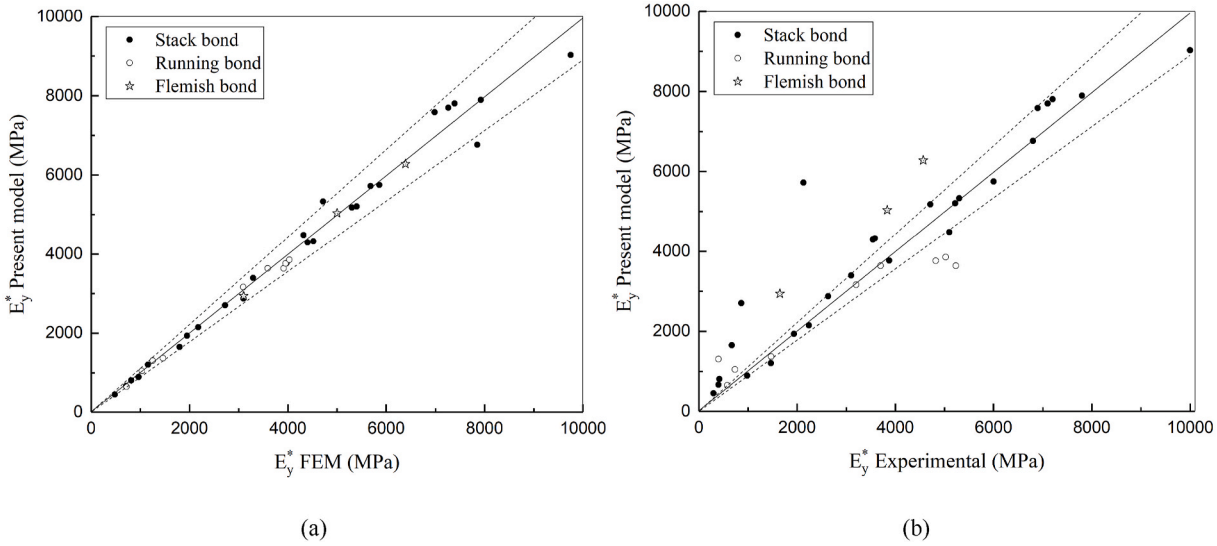

Fig. 16. Comparison of the vertical Young's modulus E_y^* between: (a) FEM and the proposed model; (b) experiments and the proposed model. (The dotted lines are 10% deviation lines).

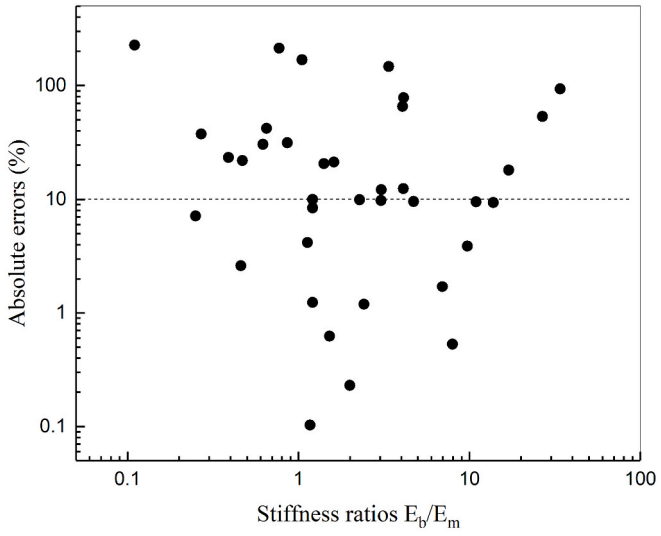

Fig. 17. Absolute errors between model results and experimental values for different stiffness ratios E_b/E_m .

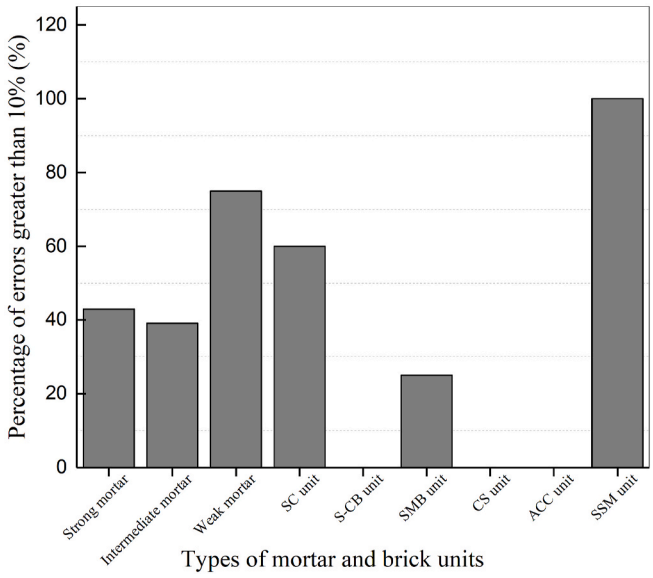

Fig. 18. Percentages of the absolute errors greater than 10% for different types of mortar and units.

potential of the proposed model for nonlinear analysis has been preliminarily demonstrated by considering different stiffness ratios between brick and mortar. It was observed that the proposed model can provide accurate predictions for the orthotropic effective stiffness tensors of masonry composites even for a large stiffness ratio of 1000 between brick and mortar. Its application within the micro-poromechanics theory is thus considered suitable for the development of an analytical-based multiscale model for masonry. Additionally, as the proposed model provides closed-form analytical expressions for the orthotropic stiffness tensor of masonry, it can be easily utilized in some of the available numerical procedures developed for the masonry nonlinear problems, such as (Drougkas and Sarhosis, 2021; Pel à et al., 2013), which involve calculating the effective (tangent/secant) stiffness tensors (matrices) of masonry in each iterative step of the nonlinear process.

Author statement

Yubao Zhou: Conceptualization, Methodology, Software, Formal analysis, Investigation, Data curation, Writing - original draft. **L.J. Sluijs**: Writing–review & editing, Supervision. **Rita Esposito**: Conceptualization, Methodology, Writing – review & editing, Supervision, Project administration, Funding acquisition.

Declaration of competing interest

The authors declare that they have no known competing financial interests or personal relationships that could have appeared to influence the work reported in this paper.

Acknowledgment

Acknowledgment is made to the China Scholarship Council (CSC) for the financial support to the first author.

Appendix

A. Eshelby tensor for elliptic cylindrical inclusions

For isotropic media, the nonzero elements of the Eshelby's tensor for elliptic cylindrical inclusions with semi-axes a, b, c ($c\to\infty$) are as follows (Weinberger et al., 2005):

$$S_{3311}=S_{3322}=S_{3333}=0$$

$$S_{1111}=\frac{1}{2(1-v)}\left[\frac{b^2+2ab}{(a+b)^2}+(1-2v)\frac{b}{a+b}\right]$$

$$S_{2222}=\frac{1}{2(1-v)}\left[\frac{a^2+2ab}{(a+b)^2}+(1-2v)\frac{a}{a+b}\right]$$

$$S_{1122}=\frac{1}{2(1-v)}\left[\frac{b^2}{(a+b)^2}-(1-2v)\frac{b}{a+b}\right]$$

$$S_{2233}=\frac{1}{2(1-v)}\frac{2va}{a+b}$$

$$S_{2211}=\frac{1}{2(1-v)}\left[\frac{a^2}{(a+b)^2}-(1-2v)\frac{a}{a+b}\right]$$

$$S_{1212}=\frac{1}{2(1-v)}\left[\frac{a^2+b^2}{2(a+b)^2}-\frac{(1-2v)}{2}\right]$$

$$S_{1133}=\frac{1}{2(1-v)}\frac{2vb}{a+b}$$

$$S_{2323}=\frac{a}{2(a+b)}$$

$$S_{3131}=\frac{b}{2(a+b)}$$

where v denotes the Poisson's ratio of the matrix phase. The semi axis a, b, and c are parallel to the coordinate x, y and z, respectively. All other components S_{ijkl} are zeros.

B. Eshelby tensor for ellipsoidal inclusions

For isotropic media, the components of Eshelby's tensor S_{ijkl} for an ellipsoid with semi-axes a, b, c are as follows (Weinberger et al., 2005):

$$S_{1112}=S_{1223}=S_{1232}=0$$

$$S_{1111}=\frac{3}{8\pi(1-v)}a^2I_{11}+\frac{1-2v}{8\pi(1-v)}I_1$$

$$S_{1122}=\frac{3}{8\pi(1-v)}b^2I_{12}+\frac{1-2v}{8\pi(1-v)}I_1$$

$$S_{1133}=\frac{3}{8\pi(1-v)}c^2I_{13}+\frac{1-2v}{8\pi(1-v)}I_1$$

$$S_{1212}=\frac{a^2+b^2}{8\pi(1-v)}I_{12}+\frac{1-2v}{8\pi(1-v)}(I_1+I_2)$$

where v is the Poisson's ratio of the matrix phase. The semi axis a, b, and c are parallel to coordinate x, y and z, respectively. Other nonzero elements can be determined by changing the subscript in the above expressions. The I_i and I_{ij} terms are expressed as follows:

$$I_1=\frac{4\pi abc}{(a^2-b^2)(a^2-c^2)^{1/2}}[F(\theta,k)-E(\theta,k)]$$

$$I_3=\frac{4\pi abc}{(b^2-c^2)(a^2-c^2)^{1/2}}\left[\frac{b(a^2-c^2)^{1/2}}{ac}-E(\theta,k)\right]$$

where

$$\theta = arcsin\sqrt{\frac{a^2 - c^2}{a^2}}$$

$$k = \sqrt{\frac{a^2 - b^2}{a^2 - c^2}}$$

and

$$I_1 + I_2 + I_3 = 4\pi$$

$$3I_{11} + I_{12} + I_{13} = \frac{4\pi}{a^2}$$

$$3a^2 I_{11} + b^2 I_{12} + c^2 I_{13} = 3I_1$$

$$I_{12} = \frac{I_1 - I_2}{a^2 - b^2}$$

and the standard elliptic integrals are expressed as follows:

$$F(\theta, k) = \int_0^{\theta} \frac{dw}{\left(1 - k^2\ sin^2\ w\right)^{1/2}}$$

$$E(\theta, k) = \int_0^{\theta} \left(1 - k^2\ sin^2\ w\right)^{1/2} dw$$

References

Adam, J.M., et al., 2010. Micromodelling of eccentrically loaded brickwork: study of masonry wallettes. Eng. Struct. 32 (5), 1244–1251.

Addessi, D., Sacco, E., 2012. A multi-scale enriched model for the analysis of masonry panels. Int. J. Solid Struct. 49 (6), 865–880.

Addessi, D., Sacco, E., Paolone, A., 2010. Cosserat model for periodic masonry deduced by nonlinear homogenization. Eur. J. Mech. Solid. 29 (4), 724–737.

Addessi, D., et al., 2020. Multiscale analysis of in-plane masonry walls accounting for degradation and frictional effects. Int. J. Multiscale Comput. Eng. 18 (2).

Addessi, D., et al., 2021. Multiscale analysis of out-of-plane masonry elements using different structural models at macro and microscale. Comput. Struct. 247, 106477.

Almeida, F.P., Cecchi, A., 2021. Mechanics of structure genome applied in the homogenization of masonry reinforced by FRP repointing technique. Comput. Struct. 253, 106576.

Almeida, F.P., Lourenço, P.B., 2020. Three-dimensional elastic properties of masonry by mechanics of structure gene. Int. J. Solid Struct. 191, 202–211.

Anthoine, A., 1995. Derivation of the in-plane elastic characteristics of masonry through homogenization theory. Int. J. Solid Struct. 32 (2), 137–163.

Barthélémy, J.-F., Dormieux, L., Kondo, D., 2003. Détermination du comportement macroscopique d'un milieu à fissures frottantes. Compt. Rendus Mec. 331 (1), 77–84.

Bati, S.B., Ranocchiai, G., Rovero, L., 1999. A micromechanical model for linear homogenization of brick masonry. Mater. Struct. 32 (1), 22–30.

Benveniste, Y., 1987. A new approach to the application of Mori-Tanaka's theory in composite materials. Mech. Mater. 6 (2), 147–157.

Binda, L., Fontana, A., Frigerio, G., 1988. Mechanical behaviour of brick masonries derived from unit and mortar characteristics. Brick and Block Masonry(8 th IBMAC) London, Elsevier Appl. Sci. 1, 205–216.

Cecchi, A., Sab, K., 2002. A multi-parameter homogenization study for modeling elastic masonry. Eur. J. Mech. Solid. 21 (2), 249–268.

Chang, L.-Z., Messali, F., Esposito, R., 2020. Capacity of unreinforced masonry walls in out-of-plane two-way bending: a review of analytical formulations. In: Structures. Elsevier.

Chang, L.-Z., Rots, J.G., Esposito, R., 2021. Influence of aspect ratio and pre-compression on force capacity of unreinforced masonry walls in out-of-plane two-way bending. Eng. Struct. 249, 113350.

Chang, L.-Z., Rots, J.G., Esposito, R., 2022. Influence of openings on two-way bending capacity of unreinforced masonry walls. J. Build. Eng. 51, 104222.

Chettah, A., et al., 2013. Localisation analysis in masonry using transformation field analysis. Eng. Fract. Mech. 110, 166–188.

D'Altri, A.M., et al., 2019. Modeling strategies for the computational analysis of unreinforced masonry structures: review and classification. Arch. Comput. Methods Eng. 1–33.

Deude, V., et al., 2002. Micromechanical approach to nonlinear poroelasticity: application to cracked rocks. J. Eng. Mech. 128 (8), 848–855.

Doghri, I., El Ghezal, M.I., Adam, L., 2016. Finite strain mean-field homogenization of composite materials with hyperelastic-plastic constituents. Int. J. Plast. 81, 40–62.

Dormieux, L., Kondo, D., Ulm, F.-J., 2006. Microporomechanics. John Wiley & Sons.

Drougkas, A., Sarhosis, V., 2021. Micro-mechanical homogenisation of three-leaf masonry walls under compression. Eng. Struct. 245, 112890.

Drougkas, A., Roca, P., Molins, C., 2015a. Numerical prediction of the behavior, strength and elasticity of masonry in compression. Eng. Struct. 90, 15–28.

Drougkas, A., Roca, P., Molins, C., 2015b. Analytical micro-modeling of masonry periodic unit cells–Elastic properties. Int. J. Solid Struct. 69, 169–188.

Drougkas, A., Roca, P., Molins, C., 2016. Compressive strength and elasticity of pure lime mortar masonry. Mater. Struct. 49 (3), 983–999.

Drougkas, A., et al., 2019. The confinement of mortar in masonry under compression: experimental data and micro-mechanical analysis. Int. J. Solid Struct. 162, 105–120.

Drugan, W.J., Willis, J.R., 1996. A micromechanics-based nonlocal constitutive equation and estimates of representative volume element size for elastic composites. J. Mech. Phys. Solid. 44 (4), 497–524.

Du, D.-X., Zheng, Q.-S., 2002. A further exploration of the interaction direct derivative (IDD) estimate for the effective properties of multiphase composites taking into account inclusion distribution. Acta Mech. 157 (1), 61–80.

Dvorak, G.J., 1992. Transformation field analysis of inelastic composite materials. Proc. Roy. Soc. Lond. Math. Phys. Sci. 437 (1900), 311–327.

Eshelby, J.D., 1957. The determination of the elastic field of an ellipsoidal inclusion, and related problems. Proc. Roy. Soc. Lond. Math. Phys. Sci. 241 (1226), 376–396.

Esposito, R., Hendriks, M.A., 2015. Simulating the deteriorating effect of the alkali-silica reaction in concrete via a micro-poro fracture mechanical model. CONCREEP 10, 118–127.

Esposito, R., Hendriks, M.A., 2016. A multiscale micromechanical approach to model the deteriorating impact of alkali-silica reaction on concrete. Cement Concr. Compos. 70, 139–152.

Ferretti, D., Michelini, E., Rosati, G., 2015. Mechanical characterization of autoclaved aerated concrete masonry subjected to in-plane loading: experimental investigation and FE modeling. Construct. Build. Mater. 98, 353–365.

Fritsch, A., Hellmich, C., Young, P., 2013. Micromechanics-derived scaling relations for poroelasticity and strength of brittle porous polycrystals. J. Appl. Mech. 80 (2).

Gumaste, K., et al., 2007. Strength and elasticity of brick masonry prisms and wallettes under compression. Mater. Struct. 40 (2), 241–253.

Hill, R., 1963. Elastic properties of reinforced solids: some theoretical principles. J. Mech. Phys. Solid. 11 (5), 357–372.

Hu, D., Tuohuti, A., 2014. Masonry homogenization micro-mechanics analysis model. In: Advanced Materials Research. Trans Tech Publ.

Jafari, S., 2021. Material Characterisation of Existing Masonry: A Strategy to Determine Strength, Stiffness and Toughness Properties for Structural Analysis. Delft University of Technology: TU Delft Applied Mechanics. Doctoral thesis. https://repository.tudelft.nl.

Jafari, S., Rots, J.G., Esposito, R., 2020. Core testing method to assess nonlinear shear-sliding behaviour of brick-mortar interfaces: a comparative experimental study. Construct. Build. Mater. 244, 118236.

Jafari, S., Rots, J.G., Esposito, R., 2022. A correlation study to support material characterisation of typical Dutch masonry structures. J. Build. Eng. 45, 103450.
Kaushik, H.B., Rai, D.C., Jain, S.K., 2007. Stress-strain characteristics of clay brick masonry under uniaxial compression. J. Mater. Civ. Eng. 19 (9), 728–739.
Klusemann, B., Svendsen, B., 2010. Homogenization methods for multi-phase elastic composites. Tech. Mech.-Eur. J. Eng. Mech. 30 (4), 374–386.
Kumar, N., et al., 2016. Homogenization of periodic masonry using self-consistent scheme and finite element method. Int. J. Comput. Methods Eng. Sci. Mech. 17 (1), 7–21.
Laws, N., 1977. The determination of stress and strain concentrations at an ellipsoidal inclusion in an anisotropic material. J. Elasticity 7 (1), 91–97.
Lielens, G., 1999. Micro-macro Modeling of Structured Materials (PhD thesis). Universite Catholique de Louvain, Louvain-la-Neuve, Belgium.
Lourenço, P.B., 1996. A matrix formulation for the elastoplastic homogenisation of layered materials. Mech. Cohesive-Frict. Mater.: Int. J. Exp. Modell. Computat. Mater. Struct. 1 (3), 273–294.
Lourenço, P.B., Rots, J.G., 1997. Multisurface interface model for analysis of masonry structures. J. Eng. Mech. 123 (7), 660–668.
Lourenco, P.B., et al., 2007. Analysis of masonry structures: review of and recent trends in homogenization techniques. Can. J. Civ. Eng. 34 (11), 1443–1457.
Ma, G., Hao, H., Lu, Y., 2001. Homogenization of masonry using numerical simulations. J. Eng. Mech. 127 (5), 421–431.
Maier, G., Nappi, A., Papa, E., 1991. Damage models for masonry as a composite material: a numerical and experimental analysis. Constitut. Laws Eng. Mater. 427–432.
Marfia, S., Sacco, E., 2012. Multiscale damage contact-friction model for periodic masonry walls. Comput. Methods Appl. Mech. Eng. 205, 189–203.
Massart, T., Peerlings, R., Geers, M., 2004. Mesoscopic modeling of failure and damage-induced anisotropy in brick masonry. Eur. J. Mech. Solid. 23 (5), 719–735.
Morin, C., Vass, V., Hellmich, C., 2017. Micromechanics of elastoplastic porous polycrystals: theory, algorithm, and application to osteonal bone. Int. J. Plast. 91, 238–267.
Mura, T., 2013. Micromechanics of Defects in Solids. Springer Science & Business Media.
Nasedkina, A.A., Rajagopal, A., 2017. Finite element homogenization of periodic block masonry by the effective moduli method. In: Advanced Materials. Springer, pp. 347–359.
Nemat-Nasser, S., Hori, M., 2013. Micromechanics: Overall Properties of Heterogeneous Materials. Elsevier.
Oliveira, D.V., Lourenço, P.B., Roca, P., 2006. Cyclic behaviour of stone and brick masonry under uniaxial compressive loading. Mater. Struct. 39 (2), 247–257.
Omairey, S.L., Dunning, P.D., Sriramula, S., 2019. Development of an ABAQUS plugin tool for periodic RVE homogenisation. Eng. Comput. 35 (2), 567–577.
Page, A.W., 1978. Finite element model for masonry. J. Struct. Div. 104 (8), 1267–1285.
Pande, G., Liang, J., Middleton, J., 1989. Equivalent elastic moduli for brick masonry. Comput. Geotech. 8 (3), 243–265.
Panizza, M., et al., 2012. Experimental investigation on bond of FRP/SRP applied to masonry prisms. In: Proceedings of 6th International Conference on FRP Composites in Civil Engineering (CICE 2012), Rome, Italy.
Pardoen, T., Hutchinson, J., 2003. Micromechanics-based model for trends in toughness of ductile metals. Acta Mater. 51 (1), 133–148.
Pelà, L., Cervera, M., Roca, P., 2013. An orthotropic damage model for the analysis of masonry structures. Construct. Build. Mater. 41, 957–967.
Pensée, V., Kondo, D., Dormieux, L., 2002. Micromechanical analysis of anisotropic damage in brittle materials. J. Eng. Mech. 128 (8), 889–897.
Pichler, B., Hellmich, C., Mang, H.A., 2007. A combined fracture-micromechanics model for tensile strain-softening in brittle materials, based on propagation of interacting microcracks. Int. J. Numer. Anal. Methods GeoMech. 31 (2), 111–132.
Pierard, O., Friebel, C., Doghri, I., 2004. Mean-field homogenization of multi-phase thermo-elastic composites: a general framework and its validation. Compos. Sci. Technol. 64 (10–11), 1587–1603.
Pietruszczak, S., Niu, X., 1992. A mathematical description of macroscopic behaviour of brick masonry. Int. J. Solid Struct. 29 (5), 531–546.
Reddy, B.V., Lal, R., Rao, K.N., 2009. Influence of joint thickness and mortar-block elastic properties on the strength and stresses developed in soil-cement block masonry. J. Mater. Civ. Eng. 21 (10), 535–542.
Rekik, A., Lebon, F., 2012. Homogenization methods for interface modeling in damaged masonry. Adv. Eng. Software 46 (1), 35–42.
Sacco, E., 2009. A nonlinear homogenization procedure for periodic masonry. Eur. J. Mech. Solid. 28 (2), 209–222.
Sacco, E., Addessi, D., Paolone, A., 2010. A nonlinear transformation field procedure for periodic masonry based on an equivalent cosserat medium. In: Advanced Materials Research. Trans Tech Publ.
Stefanou, I., Sulem, J., Vardoulakis, I., 2008. Three-dimensional Cosserat homogenization of masonry structures: elasticity. Acta Geotech. 3 (1), 71–83.
Taliercio, A., 2014. Closed-form expressions for the macroscopic in-plane elastic and creep coefficients of brick masonry. Int. J. Solid Struct. 51 (17), 2949–2963.
Ulm, F.-J., Constantinides, G., Heukamp, F.H., 2004. Is concrete a poromechanics materials?—a multiscale investigation of poroelastic properties. Mater. Struct. 37 (1), 43–58.
Venkatarama Reddy, B., Gupta, A., 2006. Strength and elastic properties of stabilized mud block masonry using cement-soil mortars. J. Mater. Civ. Eng. 18 (3), 472–476.
Vermeltfoort, A., Martens, D., Van Zijl, G., 2007. Brick–mortar interface effects on masonry under compression. Can. J. Civ. Eng. 34 (11), 1475–1485.
Wang, G., et al., 2007. Effective elastic stiffness for periodic masonry structures via eigenstrain homogenization. J. Mater. Civ. Eng. 19 (3), 269–277.
Weinberger, C., Cai, W., Barnett, D., 2005. Lecture Notes–Elasticity of Microscopic Structures. ME340–Stanford University.
Weng, G., 1990. The theoretical connection between Mori-Tanaka's theory and the Hashin-Shtrikman-Walpole bounds. Int. J. Eng. Sci. 28 (11), 1111–1120.
Xia, Z., Zhang, Y., Ellyin, F., 2003. A unified periodical boundary conditions for representative volume elements of composites and applications. Int. J. Solid Struct. 40 (8), 1907–1921.
Yang, C.X., Shen, J.M., Yang, W.J., 2012. Study on homogenization process of masonry using numerical simulation based on periodic boundary conditions. In: Applied Mechanics and Materials. Trans Tech Publ.
Zheng, Q.-S., Du, D.-X., 2001. An explicit and universally applicable estimate for the effective properties of multiphase composites which accounts for inclusion distribution. J. Mech. Phys. Solid. 49 (11), 2765–2788.
Zhou, Y., Sluijs, L.J., Esposito, R., 2022. A microporomechanical model to predict nonlinear material behavior of masonry. In: Computational Modelling of Concrete and Concrete Structures. CRC Press, pp. 363–372.
Zhu, Q.-Z., Kondo, D., Shao, J., 2008. Micromechanical analysis of coupling between anisotropic damage and friction in quasi brittle materials: role of the homogenization scheme. Int. J. Solid Struct. 45 (5), 1385–1405.
Zhu, Q.-Z., Kondo, D., Shao, J.-F., 2009. Homogenization-based analysis of anisotropic damage in brittle materials with unilateral effect and interactions between microcracks. Int. J. Numer. Anal. Methods GeoMech. 33 (6), 749–772.
Zucchini, A., Lourenço, P.B., 2002. A micro-mechanical model for the homogenisation of masonry. Int. J. Solid Struct. 39 (12), 3233–3255.